

Electroweak corrections to $W\gamma$ and $Z\gamma$ production at the LHC

E. Accomando¹, A. Denner^{2,a}, C. Meier^{2,3}

¹ Dipartimento di Fisica Teorica, Università di Torino, Via P. Giuria 1, 10125 Torino, Italy

² Paul Scherrer Institut, Würenlingen und Villigen, 5232 Villigen PSI, Switzerland

³ Institute for Theoretical Physics, University of Zürich, 8057 Zürich, Switzerland

Received: 27 September 2005 / Revised version: 25 November 2005 /
Published online: 19 April 2006 – © Springer-Verlag / Società Italiana di Fisica 2006

Abstract. We have calculated the electroweak $\mathcal{O}(\alpha)$ corrections to the processes $pp \rightarrow Z\gamma + X \rightarrow \nu_l \bar{\nu}_l \gamma + X$, $pp \rightarrow Z\gamma + X \rightarrow l\bar{l}\gamma + X$, and $pp \rightarrow W\gamma + X \rightarrow \nu_l \bar{l}\gamma + X$ at the LHC, with $l = e, \mu$ and $\nu_l = \nu_e, \nu_\mu, \nu_\tau$. The virtual corrections are evaluated in leading-pole approximation, whereas the real corrections are taken into account exactly. These corrections are implemented into a Monte Carlo generator which includes both phase-space slicing and subtraction to deal with soft and collinear singularities. We present numerical results for total cross sections as well as for experimentally interesting distributions. Applying typical LHC cuts, the electroweak corrections are of the order of -5% for the total cross sections and exceed -20% for observables dominated by high center-of-mass energies of the partonic processes.

1 Introduction

One of the primary goals of future colliders is to look for effects of theories beyond the standard model (SM). In general, there are two possibilities for new physics. Either the novel phenomena manifest themselves at energy scales probed directly at forthcoming experiments or at much larger scales. In the first case one could admire a spectacular scenario, characterized by the appearance of many new particles or resonances. In the latter case, the situation appears less favorable, but new-physics effects could still be detected in an indirect way. They can, for instance, influence physical observables at low energy by modifying the structure of the gauge-boson self-interactions. Such modifications can be parametrized in terms of anomalous couplings in the Yang–Mills vertices. While the gauge-boson couplings to the fermions have been measured at LEP2 and Tevatron to an accuracy of 0.1% – 1% [1], triple and quartic gauge-boson couplings have been determined to much lower accuracy [1, 2]. Hence, the possibility of the existence of anomalous couplings in the electroweak gauge sector cannot be ruled out yet.

Vector-boson pair-production processes turn out to be especially suited for testing the non-Abelian structure of the SM. In the last decade, their potential has been extensively exploited at LEP2 and Tevatron. For these processes, the effect of anomalous couplings is expected to rise strongly with increasing invariant mass of the gauge-boson pair, since non-standard terms lead in general to unitarity violation for longitudinal gauge bosons. At future

colliders, it will thus be worthwhile to analyze the large di-boson invariant-mass region. Another interesting property of the vector-boson pair-production processes is the so-called radiation zero, which characterizes the SM partonic amplitudes of $W\gamma$ and WZ production. Owing to gauge cancellations, for a given value of the scattering angle in the di-boson rest frame, the amplitude for $W\gamma$ production vanishes exactly and the one for WZ approximately. For hadronic processes, the resulting effect is the appearance of a dip in the angular distributions (see e.g. [3] and references therein). Any deviation from the SM gauge structure tends to modify this peculiar signature, thus providing a clean possibility to look for new physics. Present experiments are not sensitive enough to see the dip [4, 5], but the LHC offers the possibility to observe it for the first time.

Finally, the production of vector-boson pairs constitutes an important background in the search for new particles. For example, γZ production with the Z -boson decaying into a pair of neutrinos gives rise to a photon-plus-missing-energy signature. The same signal is expected for processes where the photon is produced in association with one or more heavy particles which escape the detector, either because they are weakly interacting or because they dissociate into invisible decay products. Many extensions of the SM predict the existence of such processes. For example, the ADD model [6] and related models [7, 8], where gravity becomes strong at TeV energies, predict the possibility to observe the production of a photon along with a graviton. Higher-dimensional gravitons appear as massive spin-2 neutral particles, which cannot be directly observed in a detector. Hence, graviton radiation leads to a missing-energy signature where a photon is produced with no observable particle balancing its transverse

^a e-mail: Ansgar.Denner@psi.ch

momentum. Independently of the considered new-physics model, the production of such heavy invisible particles can be inferred from the missing transverse energy distribution, which would exhibit an excess of events at high values as compared to the SM. Existing experimental searches for such an effect are, for instance, presented in [9, 10].

Owing to their limited energy and luminosity, LEP2 and Tevatron only provide weak constraints on anomalous couplings and production rates for new particles [1, 11–13].

At the LHC, the experimental collaborations will collect hundred thousands of events coming from vector-boson pair production [14]. To match the precision of the LHC experiments, the cross sections for vector-boson pair-production processes have to be calculated beyond leading order. The next-to-leading-order (NLO) QCD corrections for on-shell W and Z bosons were calculated in [15, 16] and extended to include leptonic decays in the narrow-width approximation and anomalous couplings in [17–19]. After the full NLO amplitudes including leptonic decays had become available [20], Monte Carlo programs incorporating these amplitudes have been presented for $W\gamma$ and $Z\gamma$ production in [21] and for WW , WZ , and ZZ production in [22, 23]. As a general feature, the QCD corrections modify the leading-order di-boson cross sections at the LHC by a positive amount of several tens of percent, and have thus a considerable impact on the measurement of gauge-boson couplings. At this point, the question arises if the electroweak corrections to vector-boson pair-production processes at the LHC lead to similarly sizable effects. In the above-mentioned calculations typically only universal electroweak corrections were taken into account such as the running of α or corrections associated with the ρ -parameter. This approach was based on the idea that non-universal electroweak corrections only contribute significantly in the high-energy domain, where the statistics at the LHC will be too low to extract any physics from the experimental data.

However, this is in general not the case in the high-energy region, which is of considerable experimental interest since, as discussed above, the effects of the anomalous couplings and the effects of the production of so far unknown heavy particles are most pronounced there. In fact, at high energies the electroweak corrections are enhanced by so-called electroweak Sudakov logarithms, i.e. double logarithms of the process energy over the vector-boson mass [24–28]. They can reach several tens of percent and have to be taken into account to make sure that an experimentally observed deviation from the QCD-corrected SM predictions due to electroweak effects is not misinterpreted as a signal for physics beyond the SM. The importance of the electroweak corrections to gauge-boson pair-production processes at the LHC has been confirmed by several calculations [29–31], which all point to a negative contribution of some ten percent, which well exceeds the statistical errors. Whereas the logarithmic electroweak corrections to WW , WZ , ZZ production in the high-energy limit have been calculated including the corrections to the decay process as well as the complete real corrections [31], for $W\gamma$ production only the logarithmic electroweak corrections to the production subprocess are available [29].

The electroweak corrections to $Z\gamma$ production have so far only been determined for an on-shell Z boson, i.e. without taking into account decay effects [30]. Furthermore, the real corrections for the latter two processes have been included only in the soft and collinear limits or not at all. The goal of our work is therefore the calculation of the virtual and real electroweak corrections to the cross sections and distributions for the purely leptonic channels $pp \rightarrow V\gamma + X \rightarrow l_1\bar{l}_2\gamma + X$, where $V = W, Z$. Final states containing quarks are not discussed in this work.

This paper is organized as follows: The strategy of our calculation is described in Sect. 2. In Sect. 3 we give the setup for the numerical evaluation. Numerical results are presented in Sect. 4, and Sect. 5 contains our summary. Finally, some explicit analytical results are listed in the appendices.

2 Strategy of the calculation

We consider the production of a photon along with a massive gauge boson in proton–proton collisions, where the gauge boson decays leptonically. The generic process reads

$$p + p \rightarrow V + \gamma + X \rightarrow l_3 + \bar{l}_4 + \gamma + X, \quad (1)$$

where p denotes the incoming protons, V indicates a W or Z boson, γ the outgoing photon, l_3 the outgoing lepton, \bar{l}_4 the outgoing antilepton, and X the remnants of the protons.

In the parton model, the corresponding cross section is obtained as a convolution of the distributions $\Phi_{q_1|p}$ and $\Phi_{\bar{q}_2|p}$ of the partons q_1 and \bar{q}_2 in the incoming protons with the partonic cross sections $\sigma_{q_1\bar{q}_2}$, averaged over spins and colors of the partons,

$$\sigma_{pp}(S) = \sum_{q_1, q_2} \int_0^1 dx_1 \int_0^1 dx_2 \Phi_{q_1|p}(x_1) \Phi_{\bar{q}_2|p}(x_2) \sigma_{q_1\bar{q}_2}(\hat{s}). \quad (2)$$

The sum \sum_{q_1, q_2} runs over all partonic initial states which are allowed by charge conservation. In practice we include the quarks and antiquarks $q_i = u, \bar{u}, d, \bar{d}, s, \bar{s}, c, \bar{c}$. The integration variables x_i , $i = 1, 2$ correspond to the partonic energy fractions. Moreover, the quantities S and $\hat{s} = x_1 x_2 S$ are the squared CM energies of the hadronic process and the partonic subprocesses, respectively.

For the partonic processes we adopt the generic notation

$$q_1(p_1, \sigma_1) + \bar{q}_2(p_2, \sigma_2) \rightarrow V(p_3 + p_4) + \gamma(p_5, \lambda_5) \\ \rightarrow l_3(p_3, \sigma_3) + \bar{l}_4(p_4, \sigma_4) + \gamma(p_5, \lambda_5), \quad (3)$$

where the arguments label the momenta and helicities $\sigma_i = \pm 1/2$, $i = 1, \dots, 4$ and $\lambda_5 = \pm 1$ of the corresponding particles. In the following, the masses of the external fermions are denoted by m_i , $i = 1, \dots, 4$. Since we treat all external fermions as massless these appear only as regulators of

mass singularities. The charges of the fermions are denoted by Q_i , those of the antifermions by $-Q_i$.

The lowest-order partonic cross sections are calculated using the complete matrix elements for the process

$$q_1(p_1, \sigma_1) + \bar{q}_2(p_2, \sigma_2) \rightarrow l_3(p_3, \sigma_3) + \bar{l}_4(p_4, \sigma_4) + \gamma(p_5, \lambda_5). \quad (4)$$

This means that we include the full set of Feynman diagrams, in this way accounting for all irreducible background coming from non-resonant contributions. Analytic results are given in Appendix A.1.

The electroweak radiative corrections to (4) consist of virtual corrections, resulting from loop diagrams, as well as of real corrections, originating from the process

$$q_1(p_1, \sigma_1) + \bar{q}_2(p_2, \sigma_2) \rightarrow l_3(p_3, \sigma_3) + \bar{l}_4(p_4, \sigma_4) + \gamma(p_5, \lambda_5) + \gamma(p_6, \lambda_6), \quad (5)$$

with an additional photon with momentum p_6 and helicity $\lambda_6 = \pm 1$. Virtual and real corrections have to be combined properly in order to ensure the cancellations of soft and collinear singularities (cf. Sect. 2.2). The helicity matrix elements for the process (5) are listed in Appendix A.3. For the calculation of the radiative corrections we follow the approach used for the process $e^+e^- \rightarrow W^+W^- \rightarrow 4f$ in [32]: The virtual corrections are calculated in the leading-pole approximation (LPA), i.e. we take only those terms into account that are enhanced by a resonant massive gauge-boson propagator (cf. Sect. 2.3), whereas the real corrections are calculated from the full matrix elements for the processes (5).

2.1 Absorption of initial-state mass singularities in parton distribution functions

At next-to-leading order in electroweak perturbation theory, the partonic cross sections generally contain universal, initial-state collinear singularities. The latter can be absorbed in the parton distribution functions (PDFs). To this end, one has to fix a factorization scheme, and we choose the $\overline{\text{MS}}$ scheme, which defines the connection between the lowest-order PDFs in (2) and the experimentally determined PDFs as [33, 34]

$$\begin{aligned} \bar{\Phi}_{q_i|p}(x_i) &= \bar{\Phi}_{q_i|p}^{\overline{\text{MS}}}(x_i, Q^2) - \frac{\alpha}{2\pi} Q_i^2 \int_{x_i}^1 \frac{dz}{z} \bar{\Phi}_{q_i|p}^{\overline{\text{MS}}}\left(\frac{x_i}{z}, Q^2\right) \\ &\times \left[\frac{1+z^2}{1-z} \left(\ln\left(\frac{Q^2}{m_i^2}\right) - 2 \ln(1-z) - 1 \right) \right]_+ . \end{aligned} \quad (6)$$

Here, we used the (+)-prescription

$$\begin{aligned} \int_a^1 dx [f(x)]_+ g(x) &= \int_a^1 dx f(x) [g(x) - g(1)] \\ &- g(1) \int_0^a dx f(x), \end{aligned} \quad (7)$$

and the quantity Q denotes the electromagnetic factorization scale, which should be set equal to the typical energy

scale of the considered process. Inserting the $\overline{\text{MS}}$ definition (6) into the hadronic cross section (2) allows one to write the latter as a convolution of the experimentally defined PDFs with the subtracted partonic cross section

$$\begin{aligned} \sigma_{pp}(S, Q^2) &= \sum_{q_1, q_2} \int_0^1 dx_1 \int_0^1 dx_2 \bar{\Phi}_{q_1|p}^{\overline{\text{MS}}}(x_1, Q^2) \\ &\times \bar{\Phi}_{q_2|p}^{\overline{\text{MS}}}(x_2, Q^2) \sigma_{q_1 \bar{q}_2}^{\overline{\text{MS}}}(\hat{s}, Q^2), \end{aligned} \quad (8)$$

where

$$\sigma_{q_1 \bar{q}_2}^{\overline{\text{MS}}}(\hat{s}, Q^2) = \sigma_{q_1 \bar{q}_2}(\hat{s}) - \sigma_{q_1 \bar{q}_2, \text{sing}}^{\overline{\text{MS}}}(\hat{s}, Q^2) + \mathcal{O}(\alpha^2) \quad (9)$$

and

$$\begin{aligned} \sigma_{q_1 \bar{q}_2, \text{sing}}^{\overline{\text{MS}}}(\hat{s}, Q^2) &= \\ &\frac{\alpha}{4\pi \hat{s}} \sum_{i=1,2} Q_i^2 \int_0^1 dz \int d\Phi_i(z) \left| \mathcal{M}_{q_1 \bar{q}_2}^{(0)}(\Phi_i(z)) \right|^2 \\ &\times \frac{1}{z} \left[\frac{1+z^2}{1-z} \left(\ln\left(\frac{Q^2}{m_i^2}\right) - 2 \ln(1-z) - 1 \right) \right]_+ . \end{aligned} \quad (10)$$

Here $\mathcal{M}_{q_1 \bar{q}_2}^{(0)}$ denotes the lowest-order matrix element, and $\Phi_i(z)$ represents the partonic phase-space where the incoming particle i has momentum $z p_i$. After the subtraction, the resulting cross section is free from collinear and soft singularities.

A fully consistent inclusion of the electroweak corrections into the calculation of the hadronic cross sections requires the use of PDFs in which both photonic initial states and QED $\mathcal{O}(\alpha)$ corrections are taken into account. A first global analysis of parton distributions incorporating QED contributions has been performed recently in [35]. It turns out that the photon PDFs are quite small [35], and the QED corrections change the PDFs of the quarks by less than 1% [36, 37]. These effects are below the typical uncertainty of hadronic processes and below the envisaged accuracy of our analysis. Accordingly, we restrict our calculation to initial states containing quarks and use only QCD-corrected PDFs in (8). We nevertheless investigated the dependence of our results on the electromagnetic factorization scale Q entering in (10), keeping the QCD factorization scale Q that enters $\bar{\Phi}_{q_i|p}^{\overline{\text{MS}}}(x_i, Q^2)$ in (8) fixed. For γZ production, a variation of Q by a factor 10 resulted in a change of the total cross section by less than 0.3%, of the γZ invariant-mass distribution at large invariant mass by less than 0.5%, and of the transverse-momentum distribution of the photon at large transverse momenta by less than 1%.

2.2 Treatment of soft and collinear photon emission

In first-order electroweak perturbation theory, the subtracted partonic cross section receives contributions from the lowest order, the virtual corrections, the real corrections, as well as from the term (10) arising from the factor-

ization of the initial-state collinear singularities:

$$\begin{aligned} \sigma_{q_1\bar{q}_2}^{\overline{\text{MS}}}(\hat{s}, Q^2) &= \sigma_{q_1\bar{q}_2}^{(0)}(\hat{s}) + \sigma_{q_1\bar{q}_2}^{\text{virt}}(\hat{s}) \\ &\quad + \sigma_{q_1\bar{q}_2}^{\text{real}}(\hat{s}) - \sigma_{q_1\bar{q}_2, \text{sing}}^{\overline{\text{MS}}}(\hat{s}, Q^2). \end{aligned} \quad (11)$$

In general, virtual and real corrections contain soft as well as collinear singularities, which we regularize by introducing an infinitesimal photon mass m_γ as well as small mass parameters m_i for the external fermions. These logarithmic singularities cancel when adding real and virtual corrections, except for the collinear logarithms arising from the initial state, which are absorbed in the PDFs as described in Sect. 2.1. Thus, all soft and collinear singularities cancel in (11), leaving the subtracted cross section free of any mass regulators.

However, this cancellation requires a careful treatment of soft and collinear singularities. In our work, we adopt the approach to divide the virtual and real corrections into finite and singular parts, and to cancel the dependence on the mass regulators by adding the singular parts analytically. To extract the singular parts from the real corrections, we employ two independent methods, the phase-space-slicing technique and the dipole subtraction method. In the following we give explicit expressions for our treatment of infrared, i.e. soft and collinear, singularities.

2.2.1 Finite virtual corrections

First, we define the finite virtual corrections by

$$\begin{aligned} \sigma_{q_1\bar{q}_2, \text{finite}}^{\text{virt}}(\hat{s}) &= \\ &\frac{1}{2\hat{s}} \int d\Phi_0 \times \left(2 \text{Re} \left[\mathcal{M}_{q_1\bar{q}_2}^{(0)}(\Phi_0) (\delta\mathcal{M}_{q_1\bar{q}_2}^{\text{virt}}(\Phi_0))^* \right] \right. \\ &\quad \left. - 2 \text{Re} \left[\mathcal{M}_{q_1\bar{q}_2}^{(0)}(\Phi_0) (\delta\mathcal{M}_{q_1\bar{q}_2, \text{sing}}^{\text{virt}}(\Phi_0))^* \right] \right), \end{aligned} \quad (12)$$

where $\mathcal{M}_{q_1\bar{q}_2}^{(0)}$ and $\delta\mathcal{M}_{q_1\bar{q}_2}^{\text{virt}}$ denote the matrix elements of the Born process and the corresponding electroweak virtual corrections, respectively, whereas Φ_0 is the phase-space for the Born process (4). The subtracted singular parts are given by [32, 38]

$$\begin{aligned} 2 \text{Re} \left[\mathcal{M}_{q_1\bar{q}_2}^{(0)}(\Phi_0) (\delta\mathcal{M}_{q_1\bar{q}_2, \text{sing}}^{\text{virt}}(\Phi_0))^* \right] &= \\ \frac{\alpha}{2\pi} \sum_{\substack{i,j=1 \\ i \neq j}}^n \tau_i \tau_j Q_i Q_j \left| \mathcal{M}_{q_1\bar{q}_2}^{(0)}(\Phi_0) \right|^2 &\left(\mathcal{L}(s_{ij}, m_i^2) + C_{ij} \right), \end{aligned} \quad (13)$$

where n is the number of external particles of the lowest-order process, $s_{ij} = (p_i + p_j)^2$, and $\tau_i = 1$ for incoming particles and outgoing antiparticles, whereas $\tau_i = -1$ for outgoing particles and incoming antiparticles. The singularities are contained in

$$\begin{aligned} \mathcal{L}(s_{ij}, m_i^2) &= \ln \left(\frac{m_\gamma^2}{s_{ij}} \right) \left(1 + \ln \left(\frac{m_i^2}{s_{ij}} \right) \right) \\ &\quad - \frac{1}{2} \ln^2 \left(\frac{m_i^2}{s_{ij}} \right) + \frac{1}{2} \ln \left(\frac{m_i^2}{s_{ij}} \right), \end{aligned} \quad (14)$$

while the finite parts C_{ij} are added for later convenience and distinguish between incoming, $i, j = 1, 2$, and outgoing

particles, $i, j > 2$,

$$C_{ij} = \begin{cases} -\frac{\pi^2}{3} + \frac{3}{2}, & i, j > 2, \quad i \neq j, \\ \frac{\pi^2}{6} - 1, & i = 1, 2, \quad j > 2, \\ -\frac{\pi^2}{2} + \frac{3}{2}, & i > 2, \quad j = 1, 2, \\ -\frac{\pi^2}{3} + 2, & i = 1, 2, \quad j = 1, 2, \quad i \neq j. \end{cases} \quad (15)$$

2.2.2 Phase-space slicing

In short, the idea of the phase-space-slicing technique is to define the finite real corrections by restricting the phase-space integration to the region where the squared amplitude of the bremsstrahlung process is finite. To this end, a technical cut δ_s on the energy E of the bremsstrahlung particle is introduced, as well as a technical cut δ_c on the angles ϑ_i of the bremsstrahlung particles with respect to all potential emitters. The finite real corrections are then given by

$$\sigma_{q_1\bar{q}_2, \text{finite}}^{\text{real, sli}}(\hat{s}) = \frac{1}{2\hat{s}} \int_{\substack{E > \delta_s \sqrt{\hat{s}}/2 \\ \cos \vartheta_i < 1 - \delta_c}} d\Phi_{\text{real}} \left| \mathcal{M}_{q_1\bar{q}_2}^{\text{real}}(\Phi_{\text{real}}) \right|^2, \quad (16)$$

where Φ_{real} and $\mathcal{M}^{\text{real}}$ denote the phase space and the matrix element of the bremsstrahlung process (5).

In the remaining singular parts of the real corrections, the momentum of the bremsstrahlung particle is integrated out, up to a remaining convolution over the momentum fraction z of the initial-state particle after bremsstrahlung emission. Here the soft and collinear singularities are again regularized by an infinitesimal photon mass m_γ and by small mass parameters m_i for the external fermions. The resulting expressions [32, 33] can be divided into a part arising from initial-state radiation and a part arising from final-state radiation. Adding them to the term (10) originating from the $\overline{\text{MS}}$ definition of the PDFs and to the singular parts (12) of the virtual corrections, all infrared singularities cancel and one obtains a finite contribution

$$\begin{aligned} \sigma_{q_1\bar{q}_2, \text{sing}}^{\text{virt+real, sli}}(\hat{s}, Q^2) &= \\ &= \sigma_{q_1\bar{q}_2, \text{sing}}^{\text{virt}}(\hat{s}) + \sigma_{q_1\bar{q}_2, \text{sing}}^{\text{real, sli}}(\hat{s}) - \sigma_{q_1\bar{q}_2, \text{sing}}^{\overline{\text{MS}}}(\hat{s}, Q^2) \\ &= \frac{1}{2\hat{s}} \int d\Phi_0 \left(\left| \mathcal{M}_{q_1\bar{q}_2, \text{sing}}^{\text{v+r, init}}(\Phi_0) \right|^2 + \left| \mathcal{M}_{q_1\bar{q}_2, \text{sing}}^{\text{v+r, final}}(\Phi_0) \right|^2 \right) \\ &\quad + \frac{1}{2\hat{s}} \sum_{i=1}^2 \int \frac{dz}{z} \int d\Phi_i(z) \left| \mathcal{M}_{q_1\bar{q}_2, \text{sing}}^{\text{v+r, init, z}}(\Phi_i(z)) \right|^2, \end{aligned} \quad (17)$$

where

$$\begin{aligned} \left| \mathcal{M}_{q_1\bar{q}_2, \text{sing}}^{\text{v+r, init}}(\Phi_0) \right|^2 &= \frac{\alpha}{2\pi} \sum_{i=1}^2 \sum_{\substack{j=1 \\ j \neq i}}^n Q_i \tau_i Q_j \tau_j \\ &\quad \times \left| \mathcal{M}_{q_1\bar{q}_2}^{(0)}(\Phi_0) \right|^2 \left[\frac{\pi^2}{3} - 2 + C_{ij} + \text{Li}_2 \left(1 - \frac{4E_i E_j}{s_{ij}} \right) \right. \\ &\quad \left. + \ln \left(\frac{\hat{s} \delta_c}{s_{ij} 2} \right) \left(\frac{3}{2} + \ln \delta_s^2 \right) + \frac{1}{2} \ln^2 \left(\frac{\hat{s}}{s_{ij}} \right) \right], \end{aligned} \quad (18)$$

$$\begin{aligned}
\left| \mathcal{M}_{q_1 \bar{q}_2, \text{sing}}^{\text{v+r, final}}(\Phi_0) \right|^2 &= \frac{\alpha}{2\pi} \sum_{i=3}^n \sum_{\substack{j=1 \\ j \neq i}}^n Q_i \tau_i Q_j \tau_j \left| \mathcal{M}_{q_1 \bar{q}_2}^{(0)}(\Phi_0) \right|^2 \\
&\times \left[\pi^2 - \frac{9}{2} + C_{ij} + \text{Li}_2 \left(1 - \frac{4E_i E_j}{s_{ij}} \right) + \ln \left(\frac{4E_i^2 \delta_c}{s_{ij} 2} \right) \right. \\
&\times \left. \left(\frac{3}{2} + \ln \left(\frac{\delta_s^2 \hat{s}}{4E_i^2} \right) \right) + \frac{1}{2} \ln^2 \left(\frac{4E_i^2}{s_{ij}} \right) \right], \quad (19)
\end{aligned}$$

$$\begin{aligned}
\left| \mathcal{M}_{q_1 \bar{q}_2, \text{sing}}^{\text{v+r, init, z}}(\Phi_i(z)) \right|^2 &= -\frac{\alpha}{2\pi} \sum_{\substack{j=1 \\ j \neq i}}^n Q_i \tau_i Q_j \tau_j \left| \mathcal{M}_{q_1 \bar{q}_2}^{(0)}(\Phi_i(z)) \right|^2 \\
&\times \left[\frac{1+z^2}{1-z} \left(\ln \left(\frac{\hat{s} \delta_c}{Q^2 2} \right) + 2 \ln(1-z) \right) + 1-z \right]_+, \quad (20)
\end{aligned}$$

Li_2 denotes the dilogarithm

$$\text{Li}_2(z) = -\int_0^z \frac{dt}{t} \ln(1-t), \quad |\text{arc}(1-z)| < \pi, \quad (21)$$

and $\Phi_i(z)$ represents the phase space where the incoming particle i has momentum $z p_i$.

2.2.3 Dipole subtraction method

In the dipole subtraction method, the finite real corrections are constructed by subtracting an auxiliary function from the squared bremsstrahlung amplitude before integrating over phase space,

$$\begin{aligned}
\sigma_{q_1 \bar{q}_2, \text{finite}}^{\text{real, sub}}(\hat{s}) &= \\
\frac{1}{2\hat{s}} \int d\Phi_{\text{real}} &\left(\left| \mathcal{M}_{q_1 \bar{q}_2}^{\text{real}}(\Phi_{\text{real}}) \right|^2 - \left| \mathcal{M}_{q_1 \bar{q}_2}^{\text{sub}}(\Phi_{\text{real}}) \right|^2 \right). \quad (22)
\end{aligned}$$

The subtracted terms are added again after partial analytic integration over the bremsstrahlung momentum. The subtraction function has to be chosen such that it cancels all soft and collinear singularities of the original integrand, so that the difference (22) can be integrated numerically without regulators for these singularities. Moreover, it has to be simple enough so that it can be integrated analytically over the singular regions of phase space. We use the process-independent *dipole subtraction formalism*, which was introduced for massless QCD in [39–41] and generalized to massive fermions in [38]. We follow the approach of [38] in the limit of small fermion masses.

In the dipole subtraction formalism the subtraction function is constructed from contributions that are labelled by ordered pairs ij of charged fermions, so-called dipoles. The fermions i and j are called emitter and spectator, respectively. In the formulation of [38] the subtraction

function reads

$$\begin{aligned}
\left| \mathcal{M}_{q_1 \bar{q}_2}^{\text{sub}}(\Phi_{\text{real}}) \right|^2 &= \\
-4\pi\alpha \sum_{n_b=5}^6 \sum_{\substack{i,j=1 \\ i \neq j}}^n \tau_i \tau_j Q_i Q_j g_{ij}^{\text{sub}}(p_i, p_j, p_{n_b}) &\left| \mathcal{M}_{q_1 \bar{q}_2}^{(0)}(\tilde{\Phi}_{0,ij}^{n_b}) \right|^2. \quad (23)
\end{aligned}$$

The sum over $n_b = 5, 6$ accounts for the fact that the photon appears twice in the final state of the bremsstrahlung process (5), such that a separate subtraction term has to be introduced for each final-state photon. Note that one of the two final-state photons has always to be visible in the detector and thus does not give rise to singularities. In what follows, we suppress the dependence of the phase space on n_b and denote the bremsstrahlung momentum by $k = p_{n_b}$. The phase spaces $\tilde{\Phi}_{0,ij}^{n_b}$ in (23) are given by embedding prescriptions of the phase space Φ^{real} of the bremsstrahlung process in the phase space Φ_0 of the Born process. Both the embedding prescription $\tilde{\Phi}_{0,ij}^{n_b}$ and the subtraction functions g_{ij}^{sub} depend on the emitter i and spectator j being incoming or outgoing. One therefore encounters four kinematically different cases for the subtraction functions g_{ij}^{sub} :

$$\begin{aligned}
g_{ij}^{\text{sub}}(p_i, p_j, k) &= \\
\begin{cases} \frac{1}{(p_i k)(1-y_{ij})} \left[\frac{2}{1-z_{ij}(1-y_{ij})} - 1 - z_{ij} \right], & i, j > 2, \\ \frac{1}{(p_i k)x_{ij}} \left[\frac{2}{2-x_{ij}-z_{ij}} - 1 - z_{ij} \right], & i > 2, \quad j = 1, 2, \\ \frac{1}{(p_i k)x_{ji}} \left[\frac{2}{2-x_{ji}-z_{ji}} - 1 - x_{ji} \right], & i = 1, 2, \quad j > 2, \\ \frac{1}{(p_i k)v_{ij}} \left[\frac{2}{1-v_{ij}} - 1 - v_{ij} \right], & i = 1, 2, \quad j = 1, 2, \end{cases} \quad (24)
\end{aligned}$$

where

$$\begin{aligned}
x_{ij} &= \frac{p_i p_j + p_j k - p_i k}{p_i p_j + p_j k}, \quad y_{ij} = \frac{p_i k}{p_i p_j + p_i k + p_j k}, \\
z_{ij} &= \frac{p_i p_j}{p_i p_j + p_j k}, \quad v_{ij} = \frac{p_i p_j - p_i k - p_j k}{p_i p_j}. \quad (25)
\end{aligned}$$

Denoting the number of external particles by n , one has for the embedding prescription, if both the emitter and the spectator are part of the final state,

$$\begin{aligned}
\tilde{p}_i^\mu &= p_i^\mu + k^\mu - \frac{y_{ij}}{1-y_{ij}} p_j^\mu, \quad \tilde{p}_j^\mu = \frac{1}{1-y_{ij}} p_j^\mu, \quad \tilde{p}_l^\mu = p_l^\mu, \\
i, j > 2, \quad i \neq j, \quad l = 1, \dots, n, \quad l \neq i, j, \quad (26)
\end{aligned}$$

whereas for an initial-state emitter and a final-state spectator one gets

$$\begin{aligned}
\tilde{p}_i^\mu &= x_{ji} p_i^\mu, \quad \tilde{p}_j^\mu = p_j^\mu + k^\mu - (1-x_{ji}) p_i^\mu, \quad \tilde{p}_l^\mu = p_l^\mu, \\
i = 1, 2, \quad j > 2, \quad l = 1, \dots, n, \quad l \neq i, j. \quad (27)
\end{aligned}$$

The embedding prescription for a final-state emitter and an initial-state spectator can be obtained from (27) by

exchanging $i \leftrightarrow j$ everywhere. Finally, in case of an initial-state emitter and an initial-state spectator the embedding prescription is given by

$$\begin{aligned} \tilde{p}_i^\mu &= v_{ij} p_i, \quad \tilde{p}_j = p_j, \quad \tilde{p}_l^\mu = \Lambda^\mu_\nu p_l^\nu, \quad i, j = 1, 2, \\ i \neq j, \quad l &= 3, \dots, n, \end{aligned} \quad (28)$$

with the boost matrix

$$\Lambda^\mu_\nu = g^\mu_\nu - \frac{(P_{ij} + \tilde{P}_{ij})^\mu (P_{ij} + \tilde{P}_{ij})_\nu}{P_{ij}^2 + P_{ij} \tilde{P}_{ij}} + \frac{2\tilde{P}_{ij}^\mu P_{ij,\nu}}{P_{ij}^2}. \quad (29)$$

Here, \tilde{P}_{ij} represents the total initial-state momentum after the projection, $\tilde{P}_{ij}^\mu = \tilde{p}_i^\mu + \tilde{p}_j^\mu$, and

$$P_{ij} = p_1 + p_2 - k = \sum_{k=3}^n p_k. \quad (30)$$

The subtracted contribution can be integrated over the (singular) photonic degrees of freedom up to a remaining convolution over a variable z . In this integration the regulators m_γ and m_i must be retained, and soft and collinear singularities appear as logarithms in these mass regulators. The resulting expressions [32, 38] can again be divided into a part arising from initial-state radiation and a part arising from final-state radiation. Adding them to the term (10) originating from the $\overline{\text{MS}}$ definition of the PDFs and to the singular parts (12) of the virtual corrections, the infrared singularities cancel and one finds

$$\begin{aligned} &\sigma_{q_1 \bar{q}_2, \text{sing}}^{\text{virt+real, sub}}(\hat{s}, Q^2) \\ &= \sigma_{q_1 \bar{q}_2, \text{sing}}^{\text{virt}}(\hat{s}) + \sigma_{q_1 \bar{q}_2, \text{sing}}^{\text{real, sub}}(\hat{s}) - \sigma_{q_1 \bar{q}_2, \text{sing}}^{\overline{\text{MS}}}(\hat{s}, Q^2) \\ &= \frac{1}{2\hat{s}} \sum_{i=1}^2 \int \frac{dz}{z} \int d\Phi_i(z) \\ &\quad \times \left(\left| \mathcal{M}_{q_1 \bar{q}_2, \text{sing}}^{\text{v+r, init, z}}(\Phi_i(z)) \right|^2 + \left| \mathcal{M}_{q_1 \bar{q}_2, \text{sing}}^{\text{v+r, final, z}}(\Phi_i(z)) \right|^2 \right), \end{aligned} \quad (31)$$

where

$$\begin{aligned} &\left| \mathcal{M}_{q_1 \bar{q}_2, \text{sing}}^{\text{v+r, init, z}}(\Phi_i(z)) \right|^2 = \\ &\quad - \frac{\alpha}{2\pi} \sum_{\substack{j=1 \\ j \neq i}}^2 Q_i \tau_i Q_j \tau_j \left| \mathcal{M}_{q_1 \bar{q}_2}^{(0)}(\Phi_i(z)) \right|^2 \\ &\quad \times \left[\frac{1+z^2}{1-z} \left(\ln\left(\frac{\hat{s}}{Q^2}\right) + 2 \ln(1-z) \right) + 1-z \right]_+ - \frac{\alpha}{2\pi} \\ &\quad \times \sum_{j=3}^n Q_i \tau_i Q_j \tau_j \left| \mathcal{M}_{q_1 \bar{q}_2}^{(0)}(\Phi_i(z)) \right|^2 \left\{ \left[\frac{1+z^2}{1-z} \right]_+ \ln\left(\frac{|\tilde{s}_{ij}|}{Q^2}\right) \right. \\ &\quad \left. + \left[\frac{1+z^2}{1-z} (2 \ln(1-z) - \ln(z)) + 1-z \right. \right. \\ &\quad \left. \left. - \frac{2}{1-z} \ln(2-z) + (1+z) \ln(1-z) \right]_+ \right\}, \end{aligned} \quad (32)$$

$$\begin{aligned} &\left| \mathcal{M}_{q_1 \bar{q}_2, \text{sing}}^{\text{v+r, final, z}}(\Phi_i(z)) \right|^2 = \\ &\quad \frac{\alpha}{2\pi} Q_i \tau_i (\tau_1 Q_1 + \tau_2 Q_2) \left| \mathcal{M}_{q_1 \bar{q}_2}^{(0)}(\Phi_i(z)) \right|^2 \\ &\quad \times \left[\frac{1}{1-z} \left(2 \ln\left(\frac{2-z}{1-z}\right) - \frac{3}{2} \right) \right]_+, \end{aligned} \quad (33)$$

and $\tilde{s}_{ij} = (\tilde{p}_i + \tilde{p}_j)^2$ is determined from the momenta of the phase space $\Phi_i(z)$, i.e. $\tilde{s}_{ij} = (z p_i + p_j)^2 = z s_{ij}$. Note that the finite part (15) of the singular virtual corrections (13) has been chosen to exactly cancel the end-point parts resulting from the subtraction function (23) such that only z -dependent contributions remain in (32) and (33).

2.2.4 Master formula

Altogether, in our approach the subtracted partonic cross section, which is free of soft and collinear singularities, can be written as a sum of four different parts,

$$\begin{aligned} \sigma_{q_1 \bar{q}_2}^{\overline{\text{MS}}}(\hat{s}, Q^2) &= \sigma_{q_1 \bar{q}_2}^{(0)}(\hat{s}) + \sigma_{q_1 \bar{q}_2, \text{finite}}^{\text{virt}}(\hat{s}) \\ &\quad + \sigma_{q_1 \bar{q}_2, \text{finite}}^{\text{real}}(\hat{s}) + \sigma_{q_1 \bar{q}_2, \text{sing}}^{\text{virt+real}}(\hat{s}, Q^2), \end{aligned} \quad (34)$$

where the finite virtual corrections in the second term of the right-hand side are defined by (12). The last two terms are given by (16) and (17), respectively, if using the phase-space-slicing technique and by (22) and (31), respectively, in case of using the subtraction method.

2.3 Treatment of finite-width effects

The processes (3) involve the production and decay of an unstable particle $V = W, Z$. The corresponding propagator leads to a pole in the amplitude, which has to be regularized by incorporating the finite width of the massive vector bosons. Several methods to include finite-width effects in a perturbative calculation have been discussed in the literature [42–54].¹ The simplest approach is given by the fixed-width scheme, which corresponds to replacing the resonant propagator by one containing a constant finite width. Since the finite-width results from resummation of an incomplete set of higher-order contributions, its introduction potentially violates gauge invariance. For Born amplitudes, the effects of this violation have been shown to be numerically small in the fixed-width scheme (see e.g. [46, 48, 55, 56]) by comparing the results to those obtained with other manifestly gauge-invariant prescriptions, as e.g. the complex-mass scheme [48].

In our calculation, following the approach of [32], we adopt the fixed-width scheme to evaluate the Born cross section and the real corrections. For the virtual corrections, on the other hand, we use the LPA [32, 43, 47]. In this approximation only the leading term in an expansion about

¹ The problem of finite-width effects and gauge invariance in $W\gamma$ production has been first addressed in [45].

the resonance pole, i.e. the residue divided by the resonant propagator, is kept. Since the residue, which is related to physical amplitudes for on-shell production and decay, and the resonant propagator are gauge invariant, the LPA yields a gauge-invariant result. As all non-resonant contributions are neglected, the number of contributing diagrams is considerably reduced, and only loop integrals with up to four propagators appear. The error induced by using the LPA for the virtual corrections can be estimated to be of the order $\alpha\Gamma_V/M_V$, where M_V and Γ_V are the mass and the width of the vector boson V , respectively, and thus of the order of a few permille. This estimate was confirmed for single W production at hadron colliders in [34] and for WW production in electron positron annihilation in [57, 58]. Thus, the LPA should be more than sufficient for the considered process, as long as the resonant diagrams dominate.

Following the approach presented in [32], the virtual corrections evaluated in LPA can be further split into factorizable and non-factorizable parts, such that the finite virtual corrections can be written as

$$\begin{aligned} \sigma_{q_1\bar{q}_2,\text{finite}}^{\text{virt,LPA}}(\hat{s}) = & \frac{1}{2\hat{s}} \int d\Phi_0 \, 2 \operatorname{Re} \left[\mathcal{M}_{q_1\bar{q}_2}^{(0),\text{LPA}}(\Phi_0, \Phi_0^{\text{osh}}) \left(\delta\mathcal{M}_{q_1\bar{q}_2,\text{fac}}^{\text{virt,LPA}}(\Phi_0, \Phi_0^{\text{osh}}) \right. \right. \\ & \left. \left. + \delta\mathcal{M}_{q_1\bar{q}_2,\text{nfac}}^{\text{virt,LPA}}(\Phi_0, \Phi_0^{\text{osh}}) - \delta\mathcal{M}_{q_1\bar{q}_2,\text{sing}}^{\text{virt,LPA}}(\Phi_0, \Phi_0^{\text{osh}}) \right)^* \right]. \quad (35) \end{aligned}$$

In (35), $\mathcal{M}_{q_1\bar{q}_2}^{(0),\text{LPA}}(\Phi_0, \Phi_0^{\text{osh}})$ denotes the Born matrix element in LPA,

$$\mathcal{M}_{q_1\bar{q}_2}^{(0),\text{LPA}}(\Phi_0, \Phi_0^{\text{osh}}) = \frac{R^{(0)}(\Phi_0^{\text{osh}})}{(p_3 + p_4)^2 - M_V^2 + iM_V\Gamma_V}, \quad (36)$$

which receives contributions from all Born diagrams containing the resonant propagator. The residue R of the amplitude at the pole is evaluated using a phase space $\Phi_0^{\text{osh}} = \{p_i^{\text{osh}}, i = 1, \dots, 5\}$ projected on the mass-shell of the decaying particle, i.e. $(p_3^{\text{osh}} + p_4^{\text{osh}})^2 = M_V^2$. We specify our choice for the on-shell projection in Appendix B. The factorizable virtual corrections in (35) get contributions from all diagrams where the resonant propagator appears outside the loop, i.e. from diagrams that factorize into a production part, a decay part, and the resonant propagator. In LPA, they can be written as

$$\delta\mathcal{M}_{q_1\bar{q}_2,\text{fac}}^{\text{virt,LPA}}(\Phi_0, \Phi_0^{\text{osh}}) = \frac{R_{\text{fac}}^{\text{virt}}(\Phi_0^{\text{osh}}, m_\gamma)}{(p_3 + p_4)^2 - M_V^2 + iM_V\Gamma_V}, \quad (37)$$

where all soft singularities are regularized by the infinitesimal photon mass parameter m_γ .

The non-factorizable virtual corrections receive contributions from all diagrams where a massless virtual particle, in our case a photon, connects the production and decay subprocesses or one of these subprocesses to the resonance. The infrared singularities originating from photon emission off the unstable boson V are here regularized by keeping the resonant momentum off-shell wherever the on-shell limit leads to a singularity. The contribution of the

diagrams where the photon couples to the resonance are already partly contained in the factorizable virtual corrections as defined above, such that this contribution has to be subtracted from the non-factorizable corrections to avoid double counting [32]. As an advantage, the non-factorizable virtual corrections can be evaluated in the extended soft photon approximation (ESPA), which corresponds to setting the loop momentum to zero wherever this does not lead to a resonance. The non-factorizable corrections

$$\begin{aligned} \delta\mathcal{M}_{q_1\bar{q}_2,\text{nfac}}^{\text{virt,LPA}}(\Phi_0, \Phi_0^{\text{osh}}) = & \frac{R_{\text{nfac}}^{\text{virt,ESPA}}(\Phi_0^{\text{osh}}, (p_3 + p_4)^2 - M_V^2)}{(p_3 + p_4)^2 - M_V^2 + iM_V\Gamma_V} \\ = & \frac{1}{2} \mathcal{M}_{q_1\bar{q}_2}^{(0),\text{LPA}}(\Phi_0, \Phi_0^{\text{osh}}) \\ & \times \delta_{\text{nfac}}^{\text{virt}}(\Phi_0^{\text{osh}}, (p_3 + p_4)^2 - M_V^2) \quad (38) \end{aligned}$$

are then proportional to the Born matrix element in LPA. We give the analytical expression for the correction factor $\delta_{\text{nfac}}^{\text{virt}}$ in Appendix A.2.

Note that in order not to spoil the cancellation of soft and collinear singularities between the virtual corrections in LPA and the real corrections evaluated exactly, we consistently subtract in (35) the singular virtual corrections evaluated in LPA:

$$\begin{aligned} 2 \operatorname{Re} \left[\mathcal{M}_{q_1\bar{q}_2}^{(0),\text{LPA}}(\Phi_0, \Phi_0^{\text{osh}}) \left(\delta\mathcal{M}_{q_1\bar{q}_2,\text{sing}}^{\text{virt,LPA}}(\Phi_0, \Phi_0^{\text{osh}}) \right)^* \right] = \\ \frac{\alpha}{2\pi} \sum_{\substack{i,j=1 \\ i \neq j}}^n \tau_i \tau_j Q_i Q_j \left| \mathcal{M}_{q_1\bar{q}_2}^{(0),\text{LPA}}(\Phi_0, \Phi_0^{\text{osh}}) \right|^2 \left(\mathcal{L}(s_{ij}^{\text{osh}}, m_i^2) + C_{ij} \right), \quad (39) \end{aligned}$$

but we use the exact singular virtual corrections in (17) and (31). In (39), $s_{ij}^{\text{osh}} = (p_i^{\text{osh}} + p_j^{\text{osh}})^2$, and \mathcal{L} and C_{ij} are given by (14) and (15), respectively.

2.4 Implementation

We have implemented our strategy in a Mathematica package called Pole, which works as an extension of the computer-algebra packages FeynArts3 [59] and FormCalc3.1 [60]. To be explicit, Pole extends these packages by the following features:

- amplitude generation for initial-state hadrons,
- amplitude generation for a given intermediate state to select only resonant factorizable and resonant non-factorizable diagrams,
- evaluation of the non-factorizable part of the amplitude in ESPA,
- reduction of fermion chains using the Weyl–van der Waerden formalism,
- numerical evaluation of hadronic cross sections,
- numerical evaluation of the virtual corrections in LPA,
- phase-space integration for an arbitrary number of external particles using the generic phase-space generator of Lusifer [61],

– numerical evaluation of the real corrections using phase-space-slicing or the dipole subtraction method.

The main changes for the amplitude generation are the possibility to specify hadronic initial states as well as the resonant particles in the intermediate state. The latter information is used to only generate the resonant factorizable and the resonant non-factorizable diagrams. In the FormCalc part, we have implemented the Weyl–van der Waerden formalism, which reduces the fermionic spinor structures down to Weyl-spinor products and Kronecker deltas in the helicities. Note that our implementation of the Weyl–van der Waerden method works independently of the formalism contained in FormCalc4 [62], where the fermionic structures are numerically evaluated as two-dimensional matrix–vector products. As an advantage of our approach with regard to FormCalc4, the matrix element is split into helicity amplitudes, and only non-vanishing components are calculated.

As a consequence, the kinematical dependence of the amplitudes as calculated by Pole is completely different from the amplitude given back by FormCalc3.1, so that we had to rewrite the Fortran part of FormCalc3.1. The input required by the new code are model parameters, kinematical cuts, PDF set, as well as the aforementioned on-shell projection of the outgoing momenta. Using this input, the program automatically calculates hadronic cross sections and kinematical distributions including real QED corrections as well as virtual electroweak corrections evaluated in LPA. The phase-space integration is done using the generic Monte Carlo generator of Lusifer [61], which is able to handle the kinematics of a process with an arbitrary number of final-state particles. To flatten the propagator peaks, Lusifer employs the multi-channel importance sampling [63–66] with adaptive weight optimization [67]. Since the generator was originally designed to calculate Born cross sections only, we had to extend it to incorporate an appropriate treatment of soft and collinear singularities. We implemented both the dipole subtraction method and the phase-space-slicing technique as presented in Sect. 2.2.

Pole is designed to handle processes involving an arbitrary final state and an arbitrary number of resonances. The applicability is limited to processes where the decay products are stable, i.e. it cannot handle cascade decays where unstable particles decay into unstable particles. Furthermore, the treatment of the non-factorizable corrections as well as the implementation of the phase-space-slicing and subtraction methods are limited to massless external particles.

3 Input and checks

3.1 Parameter input and process definition

We consider three classes of processes:

$$p + p \rightarrow \nu_l + \bar{\nu}_l + \gamma + X, \quad l = e, \mu, \tau, \quad (40)$$

$$p + p \rightarrow l + \bar{l} + \gamma + X, \quad l = e, \mu, \quad (41)$$

$$p + p \rightarrow \nu_l + \bar{l} + \gamma + X, \quad l = e, \mu. \quad (42)$$

The first two classes allow one to analyze $Z\gamma$ production, while the third one contains $W\gamma$ as intermediate state. In the following sections, we present results for the LHC at CM energy $\sqrt{S} = 14$ TeV and an integrated luminosity $L = 100 \text{ fb}^{-1}$ per experiment. We neglect all fermion masses except for the mass of the top quark. We nevertheless keep the fermion masses in arguments of loop integrals as regularization parameters for possible collinear divergences, where we use the values [68, 69]

$$\begin{aligned} m_u &= 0.066 \text{ GeV}, & m_c &= 1.6 \text{ GeV}, \\ m_t &= 178 \text{ GeV}, & m_d &= 0.066 \text{ GeV}, \\ m_s &= 0.15 \text{ GeV}, & m_b &= 4.9 \text{ GeV}, \\ m_e &= 5.109989 \times 10^{-4} \text{ GeV}, & m_\mu &= 0.105658369 \text{ GeV}, \\ m_\tau &= 1.77699 \text{ GeV}. \end{aligned} \quad (43)$$

For the vector-boson masses and decay widths we take [68]

$$\begin{aligned} M_W &= 80.425 \text{ GeV}, & \Gamma_W &= 2.124 \text{ GeV}, \\ M_Z &= 91.1876 \text{ GeV}, & \Gamma_Z &= 2.4952 \text{ GeV}, \end{aligned} \quad (44)$$

and the Higgs-boson mass is fixed to

$$M_H = 115 \text{ GeV}. \quad (45)$$

We use the G_μ scheme, i.e. we define the fine structure constant in terms of the Fermi constant

$$\alpha = \alpha_{G_\mu} = \frac{\sqrt{2}}{\pi} G_\mu M_W^2 s_W^2, \quad (46)$$

where the quantity $s_W^2 = 1 - M_W^2/M_Z^2$ denotes the sine of the weak mixing angle squared, and we use the value $G_\mu = 1.16637 \times 10^{-5} \text{ GeV}^{-2}$ for the Fermi constant. The definition (46) effectively resums contributions associated with the evolution of α to the W -boson mass and incorporates leading universal m_t -dependent two-loop corrections. For the coupling of one real final-state photon, we use instead the value $\alpha = \alpha(0) = 1/137.035999$, i.e. we rescale the cross section with $\alpha(0)/\alpha_{G_\mu}$. Thus we have for the lowest-order cross section $\sigma^{(0)}$ and for the corresponding corrections $\sigma^{(1)}$:

$$\sigma^{(0)} \propto \alpha(0) \alpha_{G_\mu}^2, \quad \sigma^{(1)} \propto \alpha(0) \alpha_{G_\mu}^3. \quad (47)$$

The terms absorbed in α_{G_μ} have to be subtracted from the finite virtual corrections (35) calculated in the $\alpha(0)$ scheme, once for each vertex parametrized by α_{G_μ} , to avoid double counting. Since in our case we have two such couplings in the lowest-order cross section, the finite virtual corrections are evaluated according to

$$\sigma_{q_1 \bar{q}_2, \text{finite}, \alpha_{G_\mu}}^{\text{virt, LPA}}(\hat{s}) = \sigma_{q_1 \bar{q}_2, \text{finite}}^{\text{virt, LPA}}(\hat{s}) - 2\sigma_{q_1 \bar{q}_2}^{(0), \text{LPA}}(\hat{s}) \Delta r^{(1)}. \quad (48)$$

The one-loop contribution $\Delta r^{(1)}$ to Δr can for instance be found in [70].

We neglect all loop corrections to the quark mixing, and simply multiply the cross sections of the partonic sub-processes with the squares of the quark-mixing matrix elements

$$\begin{aligned} V_{ud} &= 0.974, & V_{us} &= \sqrt{1 - V_{ud}^2}, \\ V_{ub} &= 0, & V_{cd} &= -\sqrt{1 - V_{ud}^2}, \\ V_{cs} &= 0.974, & V_{cb} &= 0, \\ V_{td} &= 0, & V_{tc} &= 0, \\ V_{tb} &= 1, \end{aligned} \quad (49)$$

for $W\gamma$ -production processes.

Following our discussion at the end of Sect. 2.1, we neglect the QED corrections to the PDFs. We therefore choose the only QCD-corrected CTEQ6M set [71] to calculate the hadronic cross sections and we neglect all contributions of the initial states containing bottom quarks. Denoting the momenta of the incoming protons by $P_{1,2}$ and the final-state momenta collectively by p_{fin} , the hadronic cross section for the $Z\gamma$ -production processes (40) and (41) can be written as

$$\begin{aligned} \sigma_{pp}(S, Q^2) &= \int_0^1 dx_1 \int_0^1 dx_2 \frac{1}{2x_1 x_2 S} \int d\Phi(p_{\text{fin}}) \sum_{q=u,d,c,s} \\ &\times \left(|\mathcal{M}_{q\bar{q}}(x_1 P_1, x_2 P_2, p_{\text{fin}})|^2 \overline{\Phi}_{q|p}^{\overline{\text{MS}}}(x_1, Q^2) \right. \\ &\times \overline{\Phi}_{\bar{q}|p}^{\overline{\text{MS}}}(x_2, Q^2) + |\mathcal{M}_{q\bar{q}}(x_2 P_2, x_1 P_1, p_{\text{fin}})|^2 \\ &\times \overline{\Phi}_{q|p}^{\overline{\text{MS}}}(x_2, Q^2) \overline{\Phi}_{\bar{q}|p}^{\overline{\text{MS}}}(x_1, Q^2) \left. \right), \end{aligned} \quad (50)$$

and we use $\mathcal{M}_{c\bar{c}} = \mathcal{M}_{u\bar{u}}$ and $\mathcal{M}_{s\bar{s}} = \mathcal{M}_{d\bar{d}}$ in the zero mass limit for the external fermions. For the $W\gamma$ -production process (42), the effects of the quark mixing are taken into account by setting the quark-mixing matrix to the unit matrix for the calculation of the amplitudes, and by convoluting the squared amplitudes according to

$$\begin{aligned} \sigma_{pp}(S, Q^2) &= \int_0^1 dx_1 \int_0^1 dx_2 \frac{1}{2x_1 x_2 S} \int d\Phi(p_{\text{fin}}) \sum_{q=u,c} \sum_{q'=d,s} |V_{qq'}|^2 \\ &\times \left(|\mathcal{M}_{q\bar{q}'}(x_1 P_1, x_2 P_2, p_{\text{fin}})|^2 \overline{\Phi}_{q|p}^{\overline{\text{MS}}}(x_1, Q^2) \overline{\Phi}_{\bar{q}'|p}^{\overline{\text{MS}}}(x_2, Q^2) \right. \\ &+ |\mathcal{M}_{q\bar{q}'}(x_2 P_2, x_1 P_1, p_{\text{fin}})|^2 \overline{\Phi}_{q|p}^{\overline{\text{MS}}}(x_2, Q^2) \overline{\Phi}_{\bar{q}'|p}^{\overline{\text{MS}}}(x_1, Q^2) \left. \right), \end{aligned} \quad (51)$$

and we use $\mathcal{M}_{u\bar{d}} = \mathcal{M}_{u\bar{s}} = \mathcal{M}_{c\bar{d}} = \mathcal{M}_{c\bar{s}}$ for unit quark-mixing matrix.

Finally, for the typical energy scale Q used to evaluate the PDFs we choose [14]

$$Q^2 = \frac{1}{2} (M_V^2 + p_{T,V}^2 + p_{T,\gamma}^2), \quad V = Z, W, \quad (52)$$

where $p_{T,V}$ denotes the transverse momentum of the resonance

$$p_{T,V} = \begin{cases} p_T^{\text{miss}} & \text{for } pp \rightarrow \nu_l \bar{\nu}_l \gamma, \\ \sqrt{(p_{T,x}^l + p_{T,x}^{\bar{l}})^2 + (p_{T,y}^l + p_{T,y}^{\bar{l}})^2} & \text{for } pp \rightarrow \bar{l} \bar{l} \gamma, \\ \sqrt{(p_{T,x}^l + p_{T,x}^{\text{miss}})^2 + (p_{T,y}^l + p_{T,y}^{\text{miss}})^2} & \text{for } pp \rightarrow \nu_l \bar{l} \gamma. \end{cases} \quad (53)$$

The missing transverse momentum p_T^{miss} is here defined as the sum of the transverse momenta of all particles visible in the detector, whereas $p_{T,x}^{\text{miss}}$ and $p_{T,y}^{\text{miss}}$ denote missing momentum in x and y direction, respectively. We use the same scale Q in the calculation of the electromagnetic $\overline{\text{MS}}$ subtraction term (10).

We have implemented a general set of cuts, proper for LHC analyses. In order to specify this set, we introduce the azimuthal–pseudorapidity separation between particle i and j

$$\Delta R_{ij} = \sqrt{(\eta_i - \eta_j)^2 + (\varphi_i - \varphi_j)^2}, \quad (54)$$

where φ_i is the azimuthal angle parametrizing the spatial part of the external momentum p_i , and the corresponding pseudo-rapidity

$$\eta_i = -\ln \left(\tan \frac{\theta_i}{2} \right) \quad (55)$$

is a measure of the production angle θ_i of the considered particle with respect to the beam.

In order to define observables that are free from soft and collinear singularities, we use the following recombination scheme.

- Photons close to the beam, i.e. with a rapidity $|\eta^\gamma| > \eta^{\text{rec}} = 2.5$, or with too small energy, i.e. $E^\gamma < E^{\text{rec}} = 2 \text{ GeV}$, are treated as invisible, i.e. they only contribute to the missing momentum.
- Photons with $|\eta^\gamma| < \eta^{\text{rec}} = 2.5$ and $E^\gamma > E^{\text{rec}} = 2 \text{ GeV}$ which are close to a final-state charged lepton or another photon, i.e. which fulfil $\Delta R_{\gamma i} < R^{\text{rec}} = 0.1$ for at least one $i = e, \mu, \gamma$, are recombined. This means that the momentum of the photon and the momentum p_i of the final-state charged lepton or photon for which $\Delta R_{\gamma i}$ has the lowest value are added and considered as an effective lepton or photon momentum.²
- Photons with $|\eta^\gamma| < \eta^{\text{rec}} = 2.5$, $E^\gamma > E^{\text{rec}} = 2 \text{ GeV}$, and $\Delta R_{\gamma i} > R^{\text{rec}} = 0.1$ for all $i = e, \mu, \gamma$ are treated as visible.

For the acceptance cuts, we consider an event to contribute to the cross section if the momenta for the leptons

² In our simplified analysis, we treat muons like electrons as far as recombination is concerned. In practice, they have to be treated differently (see for instance [72, 73]).

after possible photon recombination and the momentum of at least one of the visible final-state photons fulfil the following requirements:

- $p_T^\gamma > p_T^{\gamma,c} = 50$ GeV (100 GeV) for at least one photon in case of $W\gamma$ ($Z\gamma$) production,
- $p_T^l > p_T^{l,c} = 20$ GeV for all final-state charged leptons,
- $\Delta R_{ij} > R^c = 0.7$, $i, j = l, \gamma$, for the rapidity–azimuthal angle separation (54) between two charged leptons and between charged leptons and visible photons.
- $|\eta| < \eta^c = 2.5$ for at least one of the final-state photons and all final-state charged leptons.
- $p_T^{\text{miss}} > p_T^{\text{miss},c} = 50$ GeV (100 GeV) for the missing transverse momentum in case of $W\gamma$ ($Z\gamma$) production for final states containing at least one neutrino.

Furthermore, we introduce cuts on the invariant masses of the resonant gauge bosons. These cuts enhance the contributions of the gauge-boson pair-production process with respect to background diagrams and simultaneously reduce the error of the LPA. We impose the so-called reconstruction cut

$$M_Z - 20 \text{ GeV} < \sqrt{(p_3 + p_4)^2} < M_Z + 20 \text{ GeV} \quad (56)$$

on the phase space for the process (41). For the case of $W\gamma$ -production (42), the neutrino momentum is not an observable, so that one has to rely on the missing transverse momentum to restrict the squared energy of the lepton pair to the phase-space region around the resonance. To this end, a cut on the transverse mass

$$M_T^{l\nu} < M_W + 20 \text{ GeV} \quad (57)$$

is appropriate, where the transverse mass for a lepton–neutrino pair $l\nu_l$ is defined as

$$M_T^{l\nu} = \sqrt{(|p_T^{\text{miss}}| + |p_{T,l}|)^2 - (p_x^{\text{miss}} + p_{x,l})^2 - (p_y^{\text{miss}} + p_{y,l})^2}. \quad (58)$$

For the case of the Z -boson decaying into two neutrinos, see (40), none of the decay products is visible, and thus neither of the above reconstruction cuts can be imposed.

For the bremsstrahlung process the scale Q is fixed using the possibly recombined momenta as follows. If both photons are visible, we use

$$Q^2 = \frac{1}{2} (M_V^2 + p_{T,V}^2 + p_{T,\gamma_1}^2 + p_{T,\gamma_2}^2), \quad V = Z, W, \quad (59)$$

to evaluate the PDFs. If only one photon is visible, the expression used for the scale Q depends on the considered final state. For the $l\bar{l}\gamma\gamma$ final state, we reconstruct the transverse momentum of the bremsstrahlung particle from momentum conservation and use the expression (59). When the final state contains one or more neutrinos, the bremsstrahlung momentum contributes to the missing momentum and we use (52) and (53) instead.

3.2 Checks of the calculation

To check the amplitudes generated by Pole numerically, we performed an explicit paper-and-pencil calculation of the Born amplitudes, the non-factorizable virtual corrections, and the real corrections. We have listed the corresponding expressions in Appendix A. In addition, we compared the Born amplitude and the bremsstrahlung amplitude for zero width numerically to the result of Madgraph [74, 75] for some phase-space points and found complete agreement. For a check of the amplitude for the factorizable virtual corrections, we generated the diagrams for the partonic processes corresponding to (4) by means of FeynArts. We then switched off the non-resonant and non-factorizable diagrams by hand, and translated the corresponding amplitudes into Fortran code using FormCalc4. In the code thus generated, we replaced the resonant propagator by the corresponding propagator including a finite width. The resulting amplitudes were checked by comparing to the output of Pole for some set of phase-space points, as well as by comparing the integrated cross sections, yielding in each case complete agreement.

The numerical evaluation of the finite virtual corrections (35) was tested by numerically varying the UV regulator, i.e. the mass parameter μ for the dimensional regularization, the infrared regulator, i.e. the infinitesimal photon mass m_γ , and the masses of the external fermions. The finite virtual corrections were found to be completely independent of these parameters, and we fixed the UV regulator to $\mu = 1$ GeV, the infrared regulator to $m_\gamma = 1$ GeV, and the masses of the external fermions to the values listed in (43).

To check the treatment of the real corrections, we calculated the dependence of the sum of (16) and (17) on the slicing cut parameters δ_s and δ_c and compared the corresponding values to the sum of (22) and (31) obtained from the dipole subtraction method. In Fig. 1 we show the dependence on δ_s for fixed $\delta_c = 10^{-4}$ and the dependence on δ_c for fixed $\delta_s = 10^{-3}$ for the process $pp \rightarrow \nu_l \bar{l} \gamma + X$. The error bars reflect the uncertainty of the Monte Carlo integration. The cross section shows a plateau over the full considered range for δ_c , whereas the variation with δ_s leads to a plateau in the region $10^{-5} < \delta_s < 10^{-2}$. In addition, the numerical values obtained in these ranges agree with those obtained by using the subtraction method within the integration error, which we indicate in Fig. 1 by the horizontal lines. The same analysis for the other considered processes yielded similar results. For the results to be presented in the next section, we accordingly fixed the slicing cuts to $\delta_s = 10^{-3}$ and $\delta_c = 10^{-4}$.

Finally, tree-level amplitudes and phase-space integration have been tested by comparing the outcome of our code with the results obtained with the program used for the analyses in [29]. This latter code employs matrix elements generated by means of PHACT [76], a set of routines based on the helicity-amplitude formalism of [77], and an independent integration method. For the sake of comparison, the original version of the program was extended to include the $Z\gamma$ -production processes (40) and (41). The results for all three Born cross sections agree

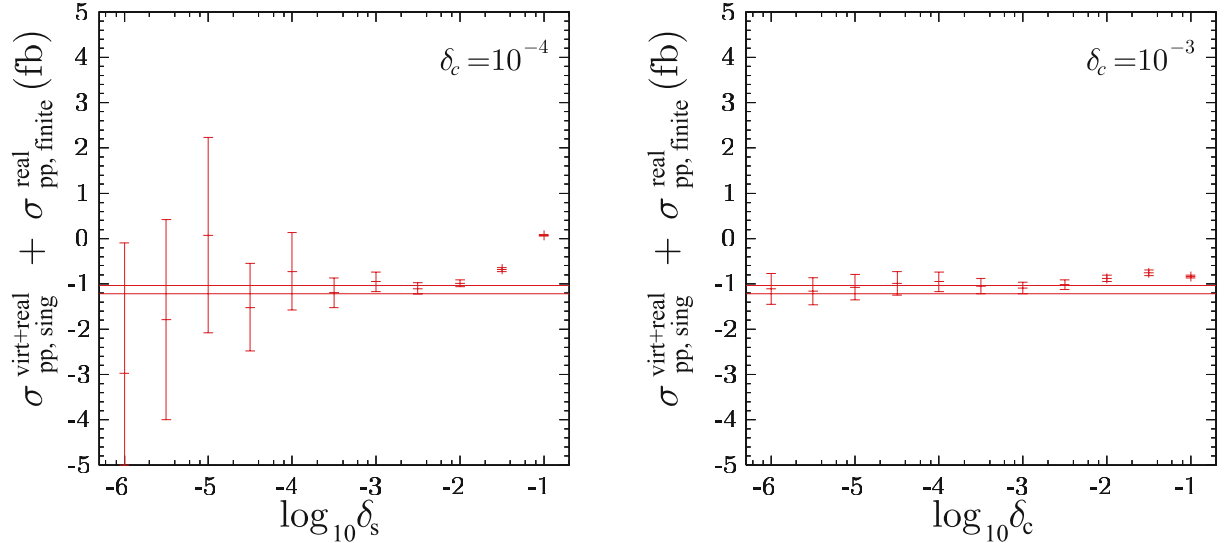


Fig. 1. Dependence of the sum of the singular virtual corrections, the complete real corrections, and the term arising from the $\overline{\text{MS}}$ definition of the PDFs for $pp \rightarrow \nu_l \bar{\nu}_l \gamma + X$ on the phase-space-slicing cut parameters. The *horizontal lines* indicate the error bars of our results obtained by using the subtraction method

at the permille level. Furthermore, we numerically cross-checked the lowest-order results for the distributions to be presented in the next section for all three processes. Complete agreement has been reached, which confirms our implementation of phase-space integration, cut routines, and histogram generation.

4 Numerical results

In this section, we illustrate the effect of the electroweak corrections on hadronic $W\gamma$ and $Z\gamma$ production at the LHC. For the process (40) we sum over all three neutrino flavors, while for the two processes (41) and (42) we include the first two lepton families only.

In the definition of the distributions for these processes, the possible presence of two photons in the final state, one coming from the real corrections, can lead to ambiguities. When observables of the final-state photon are involved, our prescription is to attribute the event weight to the bin corresponding to the photon with the largest energy.

4.1 Total cross sections

In Table 1, we show the total hadronic cross section for the three processes (40)–(42). The second column contains the lowest-order results, while the third and fourth entries display the value of the $\mathcal{O}(\alpha)$ corrections and their contribution relative to the lowest-order cross section, respectively. For the three considered processes, the electroweak corrections are negative and of the order of -2% to -7% . This is to be compared with the last column of Table 1, where we show an estimate of the statistical error based on an integrated luminosity $L = 100 \text{ fb}^{-1}$ for two experiments. As can be seen, the size of the electroweak correc-

Table 1. Total lowest-order cross section (second column) as well as the electroweak $\mathcal{O}(\alpha)$ corrections in absolute size (third column) and in percent of the lowest-order cross section (fourth column) for the three considered final states. The last column shows the statistical error for an integrated luminosity of $L = 2 \times 100 \text{ /fb}$

	$\sigma_{pp}^{(0)}$ (fb)	$\sigma_{pp}^{(1),\text{tot}}$ (fb)	$1/\sqrt{2L\sigma_{pp}^{(0)}}$ (%)	
$\nu_l \bar{\nu}_l \gamma$	212.26 (7)	−9.65 (3)	−4.5%	0.5%
$l \bar{l} \gamma$	38.99 (9)	−2.61 (7)	−6.7%	1.1%
$\nu_l \bar{l} \gamma$	124.57 (8)	−2.36 (5)	−1.9%	0.6%

tions well exceeds the statistical uncertainty. They are of the same order of magnitude as the systematic error, which is expected to be dominated by the error on the PDFs and thus presently of the order of 5% for processes initiated by quarks. The systematic uncertainty could possibly be reduced by considering ratios of cross sections. On the other hand, the size of the $\mathcal{O}(\alpha)$ corrections is strongly cut dependent and in fact increases with growing CM energy and vector-boson scattering angle. Larger values for the electroweak corrections are found by choosing, for instance, a more stringent cut on the transverse momentum of the photon. Such a constraint is useful for new-physics searches, although decreasing the statistics (see [29] and references therein). Also, distributions can be differently affected by the radiative corrections according to the specific observable at hand. In the following sections we illustrate this point for some sample variables.

4.2 Distributions for $pp \rightarrow \nu_l \bar{\nu}_l \gamma + X$

We begin by considering distributions for $pp \rightarrow \nu_l \bar{\nu}_l \gamma + X$. The error bars in the following plots result from the Monte

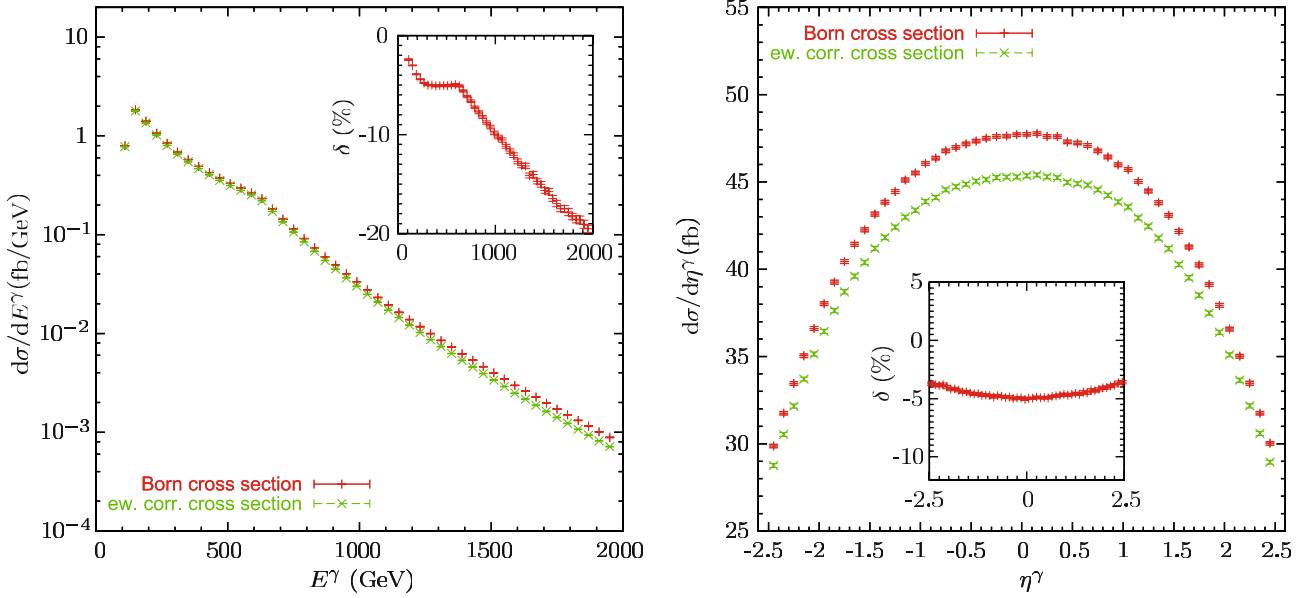


Fig. 2. Distributions in energy (*left plot*) and rapidity (*right plot*) of the final-state photon for the process $pp \rightarrow \nu_l \bar{\nu}_l \gamma + X$, $l = e, \mu, \tau$. The *inserted plots* show the relative $\mathcal{O}(\alpha)$ corrections in percent normalized to the lowest order

Carlo integration errors. In the left plot of Fig. 2, we show the energy distribution of the final-state photon. As previously mentioned, this distribution can be used to probe the existence of new particles which escape detection. These particles, once produced along with the photon, would lead to an excess of events in the high-energy domain. The kink at $E^\gamma = 600$ GeV is due to the cut $|\eta| < \eta^c$ on the rapidity of the final-state photon. This cut restricts the cosine of the photon production angle θ^γ in the laboratory frame to the interval

$$\frac{\exp^{-2\eta^c} - 1}{\exp^{-2\eta^c} + 1} < \cos \theta^\gamma < \frac{\exp^{2\eta^c} - 1}{\exp^{2\eta^c} + 1}, \quad (60)$$

so that for our choice $\eta^c = 2.5$

$$\frac{p_T^\gamma}{E^\gamma} = |\sin \theta^\gamma| > 0.163071 \dots \approx \frac{1}{6}. \quad (61)$$

Since we also applied a cut of $p_T^{\gamma,c} = 100$ GeV on the transverse momentum of the photon, this condition is always fulfilled for $E^\gamma \lesssim 600$ GeV and the rapidity cut is never applied for these photon energies. For $E^\gamma \gtrsim 600$ GeV, on the other hand, the rapidity cut will start to exclude more and more events, which leads to a steeper decrease of the Born and NLO distributions. Assuming an LHC luminosity of $L = 2 \times 100/\text{fb}$, the bin $E^\gamma = 800 \pm 10$ GeV collects a contribution of $d\sigma/dE^\gamma \approx 5 \times 10^{-2}$ fb/GeV to the total cross section and will thus contain about

$$\begin{aligned} N_{\text{ev}} &\approx L \times \frac{d\sigma}{dE^\gamma} \Delta E^\gamma = 200 \text{ fb}^{-1} \times \frac{5 \times 10^{-2} \text{ fb}}{\text{GeV}} 20 \text{ GeV} \\ &= 200 \end{aligned} \quad (62)$$

events, where $\Delta E^\gamma = 20$ GeV is the bin width. In this energy region, the electroweak corrections are of the order of -10% . The increase of the corrections with E^γ can be

attributed to large logarithms of Sudakov type. The electroweak corrections should therefore be included to match the experimental accuracy. This is the first calculation of the $\mathcal{O}(\alpha)$ corrections to the photon spectrum for $\nu_l \bar{\nu}_l \gamma$ final states. Up to now, only QCD-corrected distributions have been computed. Since the electroweak corrections reduce cross sections and distributions, considering only lowest-order or QCD-corrected results could overestimate the SM background when looking for new particles. An excess of events in the high-energy domain could then be misinterpreted as compatible with the SM predictions and could therefore be missed.

The right plot of Fig. 2 shows the distribution in the photon rapidity. The electroweak corrections are here of the order of -3% to -5% , and are thus smaller than in the case discussed above and of the order of the present systematic uncertainty from PDFs. This is because all bins receive the dominant contributions from events with low CM energies, where the electroweak corrections are small. An estimate of the event rate as in (62) applied to the bin $\eta^\gamma = 0 \pm 0.05$ gives 900 events.

4.3 Distributions for $pp \rightarrow \bar{l}l\gamma + X$

We turn now to the process (41), mediated by $Z\gamma$ production, and we show in Fig. 3 some sample distributions. The upper left plot displays the photon transverse-momentum distribution. The kink at $p_T^\gamma = 250$ GeV can be explained by the cut $\Delta R_{l\bar{l}} > R^c$ on the rapidity–azimuthal angle separation of the two leptons resulting from the Z -boson. The position of the kink is approximately given by

$$p_T^\gamma = p_T^{R^c} \equiv \frac{2M_Z}{\sqrt{2 \exp(R^c) - 1 - 1}}. \quad (63)$$

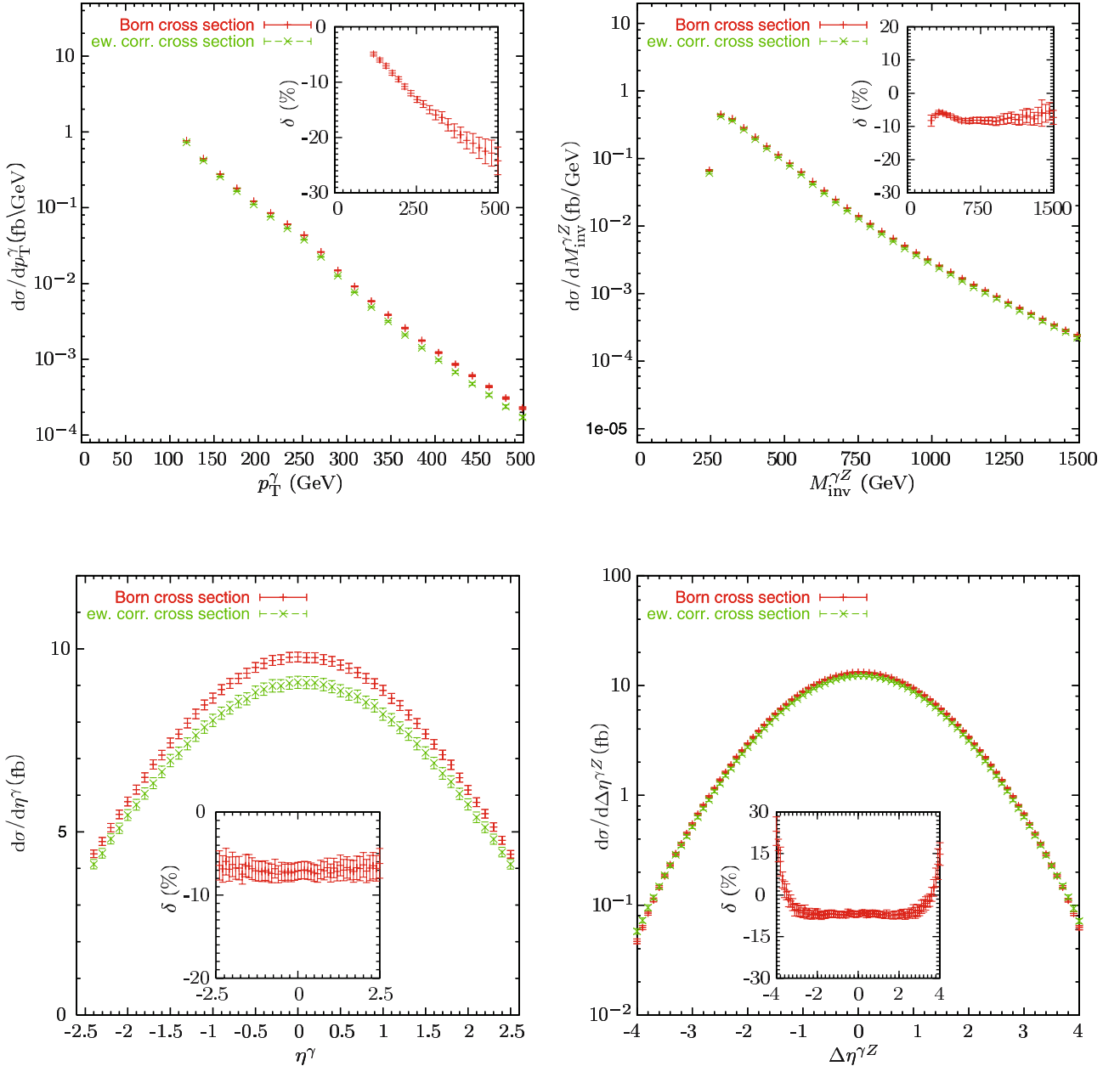


Fig. 3. Distributions in the transverse momentum of the final-state photon (*upper left plot*), in the γZ invariant mass (*upper right plot*), in the photon rapidity (*lower left plot*), and in the photon- Z -boson rapidity difference (*lower right plot*) for $pp \rightarrow l\bar{l}\gamma + X$, $l = e, \mu$. The *inserted plots* show the relative $\mathcal{O}(\alpha)$ corrections in percent normalized to the lowest order

For $p_T^Z = p_T^\gamma < p_T^{R^c}$ the R^c cut is not effective, while for $p_T^Z = p_T^\gamma > p_T^{R^c}$ the decay products of the Z -boson are so strongly boosted that this cut eliminates many of the events. The effects of the electroweak corrections to this distribution have already been studied in [30] for an on-shell final-state Z -boson, and with the real corrections included in the soft and collinear limits only. In this case, the corrections were found to be large and negative, of the order of -20% , and to increase in absolute size with rising p_T^γ . As can be seen from Fig. 3, our calculation largely confirms these results. Since the effects of the anomalous couplings are most pronounced in the high- p_T region, the elec-

troweak corrections could modify the experimental sensitivity to possible new physics. For the process considered here, the QCD corrections to the distribution in the photon transverse momentum have been calculated in [18, 19, 21]. If applying a jet veto, they are found to range between $+60\%$ and -20% [21]. At NLO, the contributions arising from electroweak and QCD corrections are thus comparable in magnitude. Including the electroweak radiative effects in the experimental analysis is therefore mandatory in order not to overestimate the SM background.

In the upper right plot of Fig. 3, we show the distribution in the final-state invariant mass. A simple estimate as in (62) shows that the process should be observable up to

$M_{\text{inv}}^{\gamma Z} = 750\text{--}1000$ GeV. As can be seen from the inset plot, the total electroweak corrections amount to roughly -8% , independently of the $M_{\text{inv}}^{\gamma Z}$ value. Electroweak radiative-correction effects are thus relevant for this important distribution. Earlier results for the electroweak corrections to the invariant-mass distribution have been published in [30] under the aforementioned approximations. Large negative corrections of the order of -15% were found, increasing in magnitude towards larger invariant masses. Comparing these results to the curve shown in the inset of the upper right plot in Fig. 3, we rather find the relative size of the virtual and real corrections approaching a plateau with rising invariant mass. We attribute this effect to angular-dependent logarithms, which are enhanced for events with photons collinear to the beams and compensate the Sudakov logarithms. Such events are eliminated by a cut on p_T^γ and thus do not influence the p_T^γ distribution, but they contribute to the invariant-mass distribution also for large invariant masses. Thus, compared to the results published in [30], the inclusion of the real corrections reduces the impact of the electroweak corrections for large invariant masses.

The distribution in the photon rapidity is shown in the lower left plot of Fig. 3. The relative size of the electroweak corrections can be seen from the inserted plot to be of the order of -7% . Finally, the photon- Z -boson rapidity difference is shown in the lower right plot of Fig. 3. While the corresponding corrections are at a similar level as for the two previous distributions in the central region, they become large and positive near $|\Delta\eta^{\gamma Z}| \approx 4$. For $|\Delta\eta^{\gamma Z}| > 5$, the cut $|\eta^\gamma| < \eta^c = 2.5$ eliminates all events with only one photon and a pair of leptons in the final state, and only bremsstrahlung events contribute. Thus, the smallness of the lowest-order cross section causes the large relative corrections near and above $|\Delta\eta^{\gamma Z}| \approx 4$. However, the event rate expected at the LHC in this region is too small for experimental observation. The remaining central part of the curve does not present novelties compared to the two previous distributions.

4.4 Distributions for $pp \rightarrow \nu_l \bar{l} \gamma + X$

Turning next to the $W\gamma$ production process, we show in Fig. 4 some distributions for $pp \rightarrow \nu_l \bar{l} \gamma + X$, $l = e, \mu$. Starting with the transverse-momentum distribution of the photon in the upper left plot, an estimate as in (62) shows that the event rate should be observable up to $p_T^\gamma = 300\text{--}400$ GeV. An analysis of the effects of the electroweak corrections on this distribution summed over $\nu_l \bar{l}$ and $l \bar{\nu}_l$ final states has already been published in [29], taking into account the W -boson decay but including only the leading logarithmic virtual corrections to the production subprocess in the high-energy approximation. Large negative corrections were found, which can reach up to -12% at $p_T^\gamma = 400$ GeV. As can be seen from the inset plot, we reproduce this result. At $p_T^\gamma = 400$ GeV, the electroweak corrections are found to contribute about -13% of the Born result, which is well above the systematic and statistical errors. The QCD corrections to the transverse-momentum distribution of the photon have been analyzed

in [21]. If applying a jet veto, large positive corrections of up to 60% for low transverse momenta have been found. They decrease to -5% to -10% of the Born cross section at $p_T^\gamma = 400$ GeV. For high transverse momenta, the electroweak corrections are thus of the same order of magnitude or even larger than the QCD corrections, and further reduce the lowest-order distribution. Again, a data analysis performed just including QCD corrections could overestimate the SM background in anomalous coupling measurements.

In the upper right plot of Fig. 4, we display our results for the distribution in the transverse mass of the final-state lepton-neutrino pair as defined in (58). The curves terminate at the cut value $M_{T,c}^{l\nu} = M_W + 20$ GeV ≈ 100.4 GeV. The W -boson resonance can be observed as a pronounced peak, an effect which could be used to determine the W -boson mass as a consistency check. The electroweak corrections can be seen from the inserted plot to contribute most at the peak, where they amount to -4% of the Born cross section.

An interesting property of angular distributions for $W\gamma$ pair production is the radiation zero, i.e. a kinematical configuration where all tree-level helicity amplitudes of the parton process are exactly zero. The radiation zero appears at

$$\cos \hat{\theta}^\gamma = \frac{Q_u + Q_d}{Q_u - Q_d} = \frac{1}{3}, \quad (64)$$

where $\hat{\theta}$ is the scattering angle of the photon in the partonic CM frame, and Q_u and Q_d denote the charge of the up quark and down quark, respectively. At the LHC, the radiation zero should be observable as a dip in the distribution in the rapidity difference between the photon and the charged lepton coming from the W -boson [3, 21]. It arises from gauge cancellations and is characteristic for the SM. As a consequence, deviations from the SM gauge structure generally tend to fill in the dip, such that an analysis of the radiation zero provides an excellent opportunity to probe new physics. QCD corrections generally enhance the cross section at the radiation zero [3]. Depending on the process definition, the effect can be quite dramatic. If no jet veto is applied, the dip arising from the radiation zero is completely washed out. If selecting only events without final-state jets, a dip at the level of 20% survives. In the bottom right plot of Fig. 4, we display our results for the distribution in the rapidity difference between the photon and the charged lepton, which exhibits the dip originating from the radiation zero at $\Delta\eta^{l\gamma} \approx 0$. The electroweak corrections hardly influence the dip and amount to about -2% . This is probably too small to have an observable impact on the data analysis. The smallness of the $\mathcal{O}(\alpha)$ correction has again its origin in the fact that a given bin receives the main contributions from the low-energy domain of phase space, where the electroweak corrections are small. Selecting kinematical regions characterized by larger energies and scattering angles would increase the size of the electroweak corrections, at the same time enhancing the radiation zero dip, as shown in [29], but decrease the statistics.

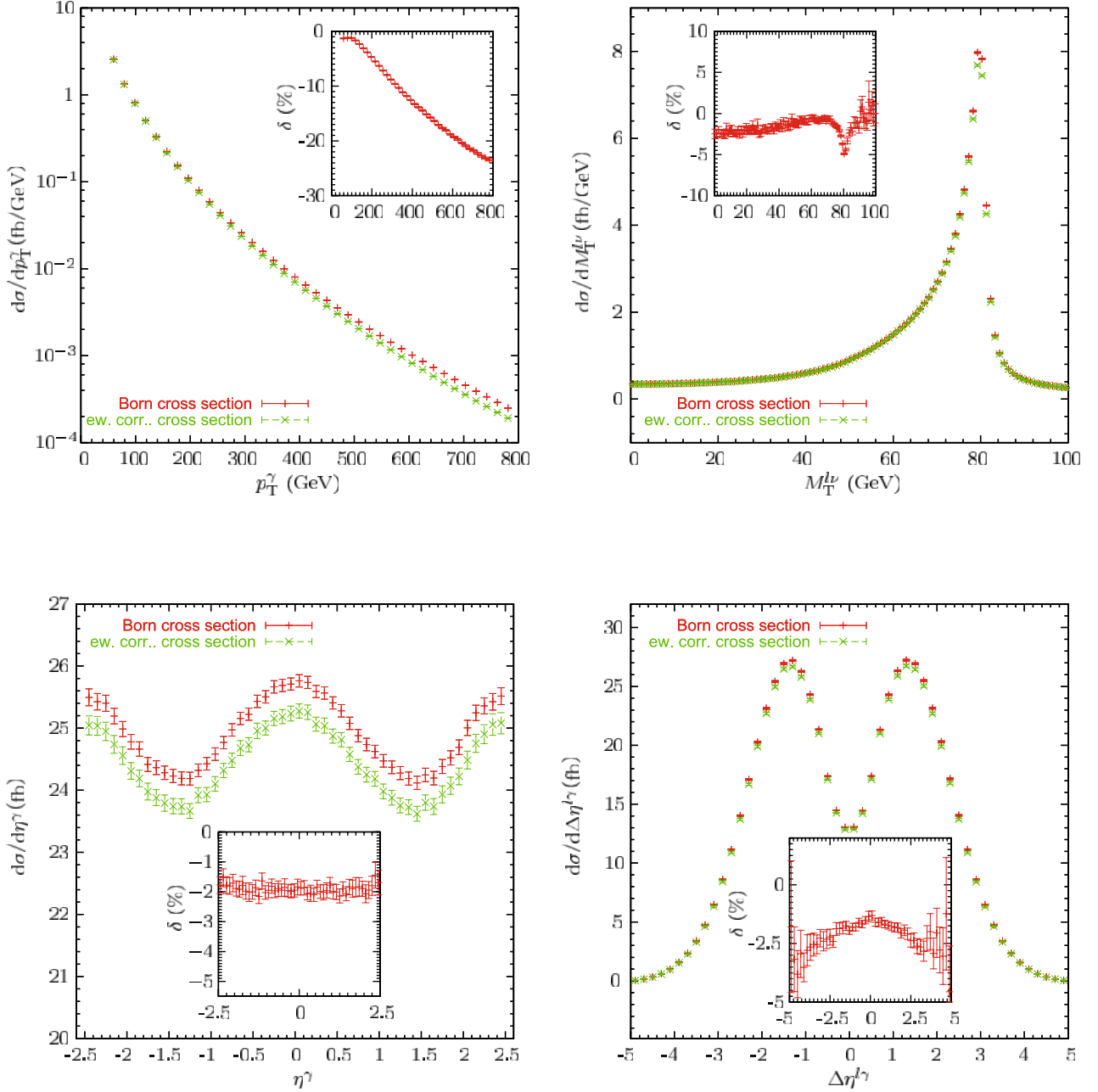


Fig. 4. Distributions in the transverse momentum of the final-state photon (*upper left plot*), in the transverse mass of the lepton–neutrino pair (*upper right plot*), in the photon rapidity (*lower left plot*) and in the lepton–photon rapidity difference (*lower right plot*) for $pp \rightarrow \nu_l \bar{l} \gamma + X$, $l = e, \mu$. The *inserted plots* show the relative electroweak corrections in percent normalized to the lowest order

Analogous remarks apply to the electroweak corrections to the photon-rapidity distribution shown in the bottom left of Fig. 4. The central peak in this distribution is caused by events with small p_T^γ and disappears if the cut $p_T^{\gamma,c} = 50$ GeV is increased. The peaks in forward and backward direction are also present for larger $p_T^{\gamma,c}$. They result from the peaking of the partonic matrix element in the direction of the incoming up quark which is additionally amplified by the boost from the CM to the laboratory system, which goes preferably along the direction of the valence quark.

4.5 Comparison with virtual correction in high-energy approximation

It is interesting to compare our results for the electroweak corrections to hadronic $W\gamma$ production with those obtained in [29]. In this latter calculation, the virtual corrections were determined for the production subprocess only and using the high-energy approximation (HEA) of [78–80]. In this approximation, all terms that vanish with M_W/\sqrt{s} at high energies are neglected, and only the logarithmic contributions to the loop integrals of the form

$\ln^2(\hat{s}/M_W^2)$, $\ln(\hat{s}/M_W^2)\ln(\hat{s}/\hat{x})$ and $\ln(\hat{s}/M_W^2)$ are taken into account, where $\hat{x} = \hat{t}, \hat{u}$ denotes one of the Mandelstam variables for the production subprocess. The use of the HEA is justified by requiring a large transverse momentum of the final-state photon, which results in large values for the partonic CM energy $\sqrt{\hat{s}}$ compared to the W -boson mass, and thus to large values for the above logarithms.

In order to tune our results to those of [29], we generated the amplitudes for the virtual corrections using Pole, but we switched off the diagrams involving the corrections to the decay subprocess. We evaluated the amplitudes thus obtained numerically by adapting the input to the parameter and cut values used in [29]. For this comparison, we moreover summed up the process (42) and its charge-conjugate, i.e. we considered both $W^+\gamma$ and $W^-\gamma$ production. The resulting numerical values for the Born cross section and the finite virtual corrections are shown in Table 2 for some values of the cut on the transverse momentum of the final-state photon. The numbers in parentheses represent the integration errors in the last digits. Note that the values shown in Table 2 do not exactly correspond to the results presented in a similar table in [29]. This is because the numbers in [29] were obtained with an incorrect implementation of the azimuthal–pseudorapidity separation (54). After correcting this error, we get in the approach of [29] the numbers given in columns 2–4 of Table 2.

The results for the Born cross section agree within errors at the permille level. Comparing our results for the finite virtual corrections to those obtained in the HEA in [29], one would expect a sizeable difference for low $p_T^{\gamma,c}$ values, which decreases for higher values of this cut to the level of 1%–2%. However, the numbers in Table 2 point rather towards a constant difference of approximately 5%–6%.

In order to understand this effect, we used the fact that Pole employs the FF-based package LoopTools [81, 82], which numerically reduces all tensorial loop integrals onto

a set of scalar basis integrals. We replaced each loop integral in this basis set by the corresponding expression in the HEA and split the latter into different contributions. The total electroweak corrections obtained in this way are smaller than those in Table 2 by at most half a percent. The subcontributions obtained with this procedure are shown in Table 3.

The electroweak logarithmic contributions in the second and third column of Table 3 result from the contributions to the basic loop integrals that involve only logarithms of the form $\ln^2(\hat{s}/M_W^2)$, $\ln(\hat{s}/M_W^2)\ln(\hat{s}/\hat{x})$, $x = \hat{t}, \hat{u}$ and $\ln(\hat{s}/M_W^2)$. This is the approximation used in [29]. As can be seen by comparing these numbers to the results in the third and fourth column in Table 2, the leading logarithmic contributions differ by about 1.2% for $p_T^{\gamma,c} = 250$ GeV and this difference decreases to the permille level for higher cut values. Thus we can reproduce the results of [29] to a satisfying accuracy by keeping only the electroweak logarithms.

The QED contributions in the fourth and fifth column of Table 3 are obtained by keeping only terms involving logarithms in the regulators for the masses of the photon and the external light fermions, i.e. logarithms of the form $\ln(m_\gamma^2/M_W^2)$ or $\ln(m_i^2/M_W^2)$, in the loop integrals and subtracting the finite virtual corrections as given in (39). We here observe a roughly energy-independent contribution of about 1.5%. This contribution results from the fact that the subtraction term (39) involves logarithms of the form $\ln(m_\gamma^2/s_{ij})$ and $\ln(m_i^2/s_{ij})$ while in the HEA they appear as $\ln(m_\gamma^2/M_W^2)$ and $\ln(m_i^2/M_W^2)$.

Finally, the contributions listed in the sixth and seventh column of Table 3 result from all remaining terms in the HEA, i.e. logarithms depending only on ratios of kinematical variables and constant terms in the high-energy expressions of the basic loop integrals, as well as extra constant terms arising from the reduction of tensor loop integral to

Table 2. Lowest-order cross section and finite virtual corrections to the production subprocess for $pp \rightarrow W^\pm\gamma + X \rightarrow l\nu_l\gamma + X$, where $l\nu_l = l\bar{\nu}_l + \bar{l}\nu_l$ and $l = e, \mu$

$p_T^{\gamma,c}$ (GeV)	Ref. [29]				this work		
	$\sigma_{pp}^{(0)}$ (fb)	$\sigma_{pp,\text{finite}}^{\text{virt}}$ (fb)	$\delta_{pp,\text{finite}}^{\text{virt}}$	$\sigma_{pp}^{(0)}$ (fb)	$\sigma_{pp,\text{finite}}^{\text{virt}}$ (fb)	$\delta_{pp,\text{finite}}^{\text{virt}}$	
250	6.01	−0.292	−4.86%	6.02 (3)	−0.649 (3)	−10.8%	
450	0.712	$−9.78 \times 10^{-2}$	−13.74%	0.711 (4)	−0.1372 (7)	−19.3%	
700	9.30×10^{-2}	$−2.06 \times 10^{-2}$	−22.12%	$9.31 (6) \times 10^{-2}$	$−2.54 (2) \times 10^{-2}$	−27.3%	
1000	1.25×10^{-2}	$−3.72 \times 10^{-3}$	−29.6%	$1.253 (9) \times 10^{-2}$	$−4.32 (3) \times 10^{-3}$	−34.5%	

Table 3. Finite virtual corrections to the production subprocess for $pp \rightarrow W^\pm\gamma + X \rightarrow l\nu_l\gamma + X$ in HEA split into electroweak logarithmic contributions $\sigma_{\text{EWLog}}^{(1)}$, the QED remnants $\Delta\sigma_{\text{QED}}^{(1)}$, as well as the remaining contributions $\sigma_{\text{rem}}^{(1)}$

$p_T^{\gamma,c}$ (GeV)	$\sigma_{\text{EWLog}}^{(1)}$ (fb)	$\delta_{\text{EWLog}}^{(1)}$	$\Delta\sigma_{\text{QED}}^{(1)}$ (fb)	$\delta_{\text{QED}}^{(1)}$	$\sigma_{\text{rem}}^{(1)}$ (fb)	$\delta_{\text{rem}}^{(1)}$
250	−0.364(1)	−6.05%	$8.6(1) \times 10^{-2}$	1.43%	−0.360(2)	−5.99%
450	−0.1026(4)	−14.4%	$1.13(2) \times 10^{-2}$	1.59%	$−4.29(2) \times 10^{-2}$	−6.04%
700	$−2.11(1) \times 10^{-2}$	−22.6%	$1.40(3) \times 10^{-3}$	1.50%	$−5.31(3) \times 10^{-3}$	−5.71%
1000	$−3.77(3) \times 10^{-3}$	−30.1%	$1.74(5) \times 10^{-4}$	1.39%	$−6.63(5) \times 10^{-4}$	−5.29%

Table 4. The non-leading contributions to the virtual corrections to the production subprocess for $pp \rightarrow W^\pm\gamma + X \rightarrow l\nu_l\gamma + X$ in HEA split up into terms $\sigma_{\text{rem,NoLog}}^{(1)}$ containing no angular-dependent logarithms, into terms $\sigma_{\text{rem,Log}}^{(1)}$ depending on single angular-dependent logarithms as well as into terms $\sigma_{\text{rem,Log}^2}^{(1)}$ depending on angular-dependent logarithms squared

p_T^c (GeV)	$\sigma_{\text{rem,NoLog}}^{(1)}$ (fb)	$\delta_{\text{rem,NoLog}}^{(1)}$	$\sigma_{\text{rem,Log}}^{(1)}$ (fb)	$\delta_{\text{rem,Log}}^{(1)}$	$\sigma_{\text{rem,Log}^2}^{(1)}$ (fb)	$\delta_{\text{rem,Log}^2}^{(1)}$
250	$-1.55(8) \times 10^{-2}$	-0.26%	-0.107(1)	-1.78%	-0.238(2)	-3.95%
450	$-4.13(8) \times 10^{-3}$	-0.58%	$1.139(2) \times 10^{-2}$	-1.97%	$-2.48(2) \times 10^{-2}$	-3.50%
700	$-6.94(9) \times 10^{-4}$	-0.74%	$-1.78(2) \times 10^{-3}$	-1.91%	$-2.83(2) \times 10^{-3}$	-3.05%
1000	$-1.09(1) \times 10^{-4}$	-0.87%	$-2.25(3) \times 10^{-4}$	-1.79%	$-3.29(3) \times 10^{-4}$	-2.62%

scalar loop integrals. These remaining terms yield a contribution of 5%–6% and thus make up the largest part of the difference between our results and those of [29].

In order to trace the origin of this large effect, we further split the remaining contributions to the basic loop integrals as shown in Table 4. The numbers in the fourth and fifth column comprise the contributions linear in the purely angular-dependent logarithms, i.e. logarithms of the form $\ln(\hat{s}/\hat{x})$, $x = \hat{t}, \hat{u}$, whereas the numbers in the sixth and seventh column correspond to the terms containing these logarithms squared. As can be seen from Table 4, the contributions linear and quadratic in the purely angular-dependent logarithms vary only little with increasing energy, but contribute with about -2% and -(3–4%), respectively, i.e. they make up the bulk of the remaining contributions. The large size of the contributions of the purely angular-dependent logarithms can be explained by the enhancement of the cross section of the considered processes in the forward and backward directions. Since in these regions \hat{s}/\hat{t} or \hat{s}/\hat{u} are small the purely angular-dependent logarithms become large. The contributions of these logarithms are the source of comparably large difference between the corrections in the HEA of [29] and the results of this paper. On the other hand, as shown in the second and third column of Table 4 the non-logarithmic remaining terms contribute to the cross section only below the percent level. The increase of this contribution with rising transverse-momentum cut of the photon can be attributed to the energy dependence of those parts of the matrix elements that have not been evaluated in the HEA.

We thus find that, for processes dominated by contributions coming from phase-space regions with small kinematical variables, the accuracy of the HEA which only takes into account enhanced logarithms of \hat{s}/M^2 may only be at the level of several percent, unless the enhanced angular-dependent logarithms are included as well.

5 Summary and conclusions

We have calculated the electroweak corrections to $Z\gamma$ and $W\gamma$ production at the LHC, with Z and W decaying into leptons. For the Born cross sections and the real corrections we use complete matrix elements. The virtual corrections are included in the leading-pole approximation. For a treatment of the soft and collinear divergences, we used

the dipole subtraction method as well as the phase-space-slicing technique.

We have implemented our strategy in a Mathematica package called Pole, which works as an extension of the programs FeynArts3 and FormCalc3.1 and is designed to calculate electroweak corrections in leading-pole approximation for hadronic or partonic processes. We have applied the program to the $pp \rightarrow \nu_l \bar{\nu}_l \gamma, l\bar{l}\gamma, \nu_l \bar{l}\gamma$ processes at the LHC, and tested the results extensively. As part of our checks we have performed a comparison with the virtual corrections evaluated in the high-energy approximation, which reveals that angular-dependent logarithms can give effects of several percent at high energies.

For the above-mentioned processes and typical LHC cuts, we find electroweak corrections of the order of -5% for total cross sections and angular distributions as, for instance, the radiation zero in $W\gamma$ production. For transverse-momentum and energy distributions, the $\mathcal{O}(\alpha)$ corrections contribute up to -20% of the lowest-order cross section. Their influence is thus well above the systematic and statistical errors, and may be of the same size as the QCD corrections or even larger, depending on the cut settings. Consequently, electroweak radiative effects have to be included in the experimental analysis when looking for the existence of anomalous vector-boson couplings or for the production of new particles via hadronic production of $Z\gamma$ and $W\gamma$. Thus, the Monte Carlo generators for LHC should include besides QCD corrections also the electroweak corrections.

Acknowledgements. We thank M. Roth for his invaluable help concerning the Monte Carlo generator and S. Dittmaier for carefully reading the manuscript. This work was supported in part by the Italian Ministero dell’Istruzione, dell’Università e della Ricerca (MIUR) under contract Decreto MIUR 26-01-2001 N.13.

Appendix A: Analytical results for the amplitudes

In this appendix, we summarize analytical results for those parts of the amplitudes that are compact enough to be explicitly displayed. We present the analytical expressions for the Born amplitude in Appendix A.1, the amplitude corresponding to the non-factorizable correc-

tions in Appendix A.2, and the amplitudes for the QED bremsstrahlung processes in A.3. The calculation of the Born and bremsstrahlung amplitudes are carried out in the framework of the Weyl–van der Waerden formalism [83, 84] as presented in [85].

A.1 The lowest-order amplitudes

The helicity amplitudes of all partonic processes (4) can be obtained from the generic set of Feynman diagrams shown in Fig. 5. The amplitude corresponding to these diagrams can be written as

$$\begin{aligned} \mathcal{M}_{c_1 c_2}^{(0) \sigma_1 \sigma_2 \sigma_3 \sigma_4 \lambda_5}(p_1, p_2, p_3, p_4, p_5) = & \\ -2\sqrt{2}e^3 \delta_{c_1 c_2} \delta_{\sigma_1 - \sigma_2} \delta_{\sigma_3 - \sigma_4} \sum_V C_{V \bar{q}_2 q_1}^{\sigma_1} C_{V \bar{f}_3 f_4}^{\sigma_3} & \\ \times B_V^{\sigma_1 \sigma_3 \lambda_5}(p_1, p_2, p_3, p_4, p_5, Q_{q_1}, Q_{q_2}, Q_{f_3}, Q_{f_4}), & \end{aligned} \quad (\text{A.1})$$

where the quantities $Q_i, i = 1, \dots, 4$ denote the charges of the external fermions (the charges of the external antifermions are given by $-Q_i$) and c_1, c_2 are the color indices for the initial-state quarks. The sum over V runs over all SM vector bosons. The non-vanishing gauge couplings $C_{V \bar{f}_a f_b}^{\pm}$ of a fermion f_b and an antifermion \bar{f}_a to the vector boson V are listed in Table 5 using the following conventions. The particle indices l (q) denote leptons (quarks). The charges and the third component of the isospin of the fermion f are denoted by Q_f and I_f^3 , respectively. The quantities s_W and c_W are the sine and the cosine of the weak mixing angle, whereas α is the fine structure constant. Finally, δ_{ij} and V_{ij} denote the Kronecker delta and the quark-mixing matrix. Note, that the elementary charge e has been extracted from the couplings.

As discussed in Sect. 2.3, the amplitude can be split into a resonant and a non-resonant part. This splitting can be done on the level of the generic functions

$$B_V^{\sigma_1 \sigma_3 \lambda_5} = B_V^{\text{res}, \sigma_1 \sigma_3 \lambda_5} + B_V^{\text{nr}, \sigma_1 \sigma_3 \lambda_5}. \quad (\text{A.2})$$

The resonant part comprises all contributions from diagrams containing the resonant propagator of the decaying

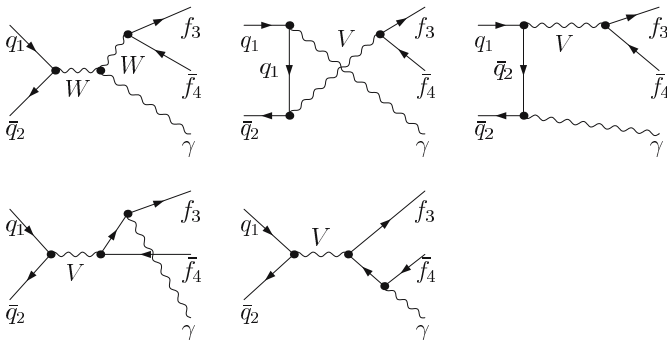


Fig. 5. Tree-level diagrams for $q_1 + \bar{q}_2 \rightarrow f_3 + \bar{f}_4 + \gamma$

Table 5. Coupling constants of quarks and leptons to the gauge bosons $V = \gamma, Z, W^\pm$

$C_{\gamma \bar{f}_2 f_1}^\pm$	$= -Q_{f_1} \delta_{f_1 f_2},$	$f_{1,2} = q, l$
$C_{Z \bar{f}_2 f_1}^\sigma$	$= \begin{cases} -\frac{s_W}{c_W} Q_{f_1} \delta_{f_1 f_2}, & \text{for } \sigma = + \\ \frac{I_{f_1}^3 - s_W^2 Q_{f_1}}{s_W c_W} \delta_{f_1 f_2}, & \text{for } \sigma = - \end{cases}$	$f_{1,2} = q, l$
$C_{W^- \bar{l} \nu_l}^\sigma$	$= \begin{cases} 0, & \text{for } \sigma = + \\ \frac{1}{\sqrt{2} s_W}, & \text{for } \sigma = - \end{cases}$	$l = e, \mu, \tau$
$C_{W^+ \bar{\nu}_l l}^\sigma$	$= \begin{cases} 0, & \text{for } \sigma = + \\ \frac{1}{\sqrt{2} s_W}, & \text{for } \sigma = - \end{cases}$	$l = e, \mu, \tau$
$C_{W^- \bar{q}_2 q_1}^\sigma$	$= \begin{cases} 0, & \text{for } \sigma = + \\ \frac{1}{\sqrt{2} s_W} V_{q_2 q_1}^\dagger, & \text{for } \sigma = - \end{cases}$	$q_1 = u, c, t \quad q_2 = d, s, b$
$C_{W^+ \bar{q}_2 q_1}^\sigma$	$= \begin{cases} 0, & \text{for } \sigma = + \\ \frac{1}{\sqrt{2} s_W} V_{q_2 q_1}, & \text{for } \sigma = - \end{cases}$	$q_1 = d, s, b \quad q_2 = u, c, t$

particle V , and thus corresponds to the amplitude originating from the diagrams in the first row of Fig. 5. Applying the Weyl–van der Waerden formalism as presented in [85] to these diagrams, the generic function for all helicities positive is given by

$$\begin{aligned} B_V^{\text{res}, +++}(p_1, p_2, p_3, p_4, p_5, Q_1, Q_2, Q_3, Q_4) = & \\ -P_V(p_3 + p_4) \frac{\langle p_1 p_4 \rangle^2}{\langle p_4 p_5 \rangle} \left\{ \frac{Q_1 \langle p_3 p_2 \rangle^*}{\langle p_1 p_5 \rangle} + \frac{Q_2 \langle p_3 p_1 \rangle^*}{\langle p_2 p_5 \rangle} \right. & \\ \left. - (Q_2 - Q_1) P_V(p_1 + p_2) \langle p_3 p_5 \rangle^* \langle p_2 p_1 \rangle^* \right\}. & \quad (\text{A.3}) \end{aligned}$$

The non-resonant part of the Born amplitude, on the other hand, receives contributions from the remaining diagrams in the second row of Fig. 5. Expressed in Weyl-spinor products, the generic function for all helicities positive reads

$$\begin{aligned} B_V^{\text{nr}, +++}(p_1, p_2, p_3, p_4, p_5, Q_1, Q_2, Q_3, Q_4) = & \\ P_V(p_1 + p_2) \frac{Q_3 \langle p_1 p_4 \rangle^2 \langle p_2 p_1 \rangle^*}{\langle p_3 p_5 \rangle \langle p_4 p_5 \rangle}. & \quad (\text{A.4}) \end{aligned}$$

Here M_V is the mass and Γ_V the decay width of the vector boson V , and the corresponding propagators are denoted as

$$P_V(k) = \frac{1}{k^2 - M_V^2 - iM_V \Gamma_V}. \quad (\text{A.5})$$

The Weyl-spinor products are defined by

$$\langle pq \rangle = 2\sqrt{p_0 q_0} \left[e^{-i\phi_p} \cos \frac{\theta_p}{2} \sin \frac{\theta_q}{2} - e^{-i\phi_q} \cos \frac{\theta_q}{2} \sin \frac{\theta_p}{2} \right], \quad (\text{A.6})$$

where θ_p, θ_q and ϕ_p, ϕ_q are the polar and azimuthal angles, respectively, of the corresponding light-like 4-momenta,

$$\begin{aligned} p^\mu &= p_0 (1, \sin \theta_p \cos \phi_p, \sin \theta_p \sin \phi_p, \cos \theta_p), \\ q^\mu &= q_0 (1, \sin \theta_q \cos \phi_q, \sin \theta_q \sin \phi_q, \cos \theta_q). \end{aligned} \quad (\text{A.7})$$

The amplitudes for neutral current reactions can be extracted from (A.3) and (A.4) by simply setting $(Q_2 - Q_1) = 0$. Inserting (A.3) and (A.4) in (A.1) and adding the resulting expressions yields the full Born amplitude. While this is gauge invariant, the resonant and non-resonant parts as defined above are gauge-dependent, unless applying the LPA. To this end, one has to set the finite width in the s -channel propagator $P_V(p_1 + p_2)$ in the resonant amplitude (A.3) to zero and to insert the resulting expression in (A.1), where the spinor and scalar products have to be evaluated using the on-shell projected momenta, except for in the resonant propagator $P_V(p_3 + p_4)$. Note that we set the gauge spinor for the external photon to $g = p_4$ to obtain the above results, which is why the contribution of the diagram with the photon coupling to the external fermion f_4 vanishes.

Dropping the superscript for resonant and non-resonant contributions in what follows, the other helicity combinations can be obtained as

$$\begin{aligned} B_V^{-++}(p_1, p_2, p_3, p_4, p_5, Q_1, Q_2, Q_3, Q_4) = & \\ & B_V^{+++}(p_2, p_1, p_3, p_4, p_5, -Q_2, -Q_1, Q_3, Q_4), \\ B_V^{+-+}(p_1, p_2, p_3, p_4, p_5, Q_1, Q_2, Q_3, Q_4) = & \\ & B_V^{+++}(p_1, p_2, p_4, p_3, p_5, Q_1, Q_2, -Q_4, -Q_3), \\ B_V^{-+-}(p_1, p_2, p_3, p_4, p_5, Q_1, Q_2, Q_3, Q_4) = & \\ & B_V^{+++}(p_2, p_1, p_4, p_3, p_5, -Q_2, -Q_1, -Q_4, -Q_3), \end{aligned} \quad (\text{A.8})$$

as well as

$$B_V^{\sigma_1\sigma_3-}(p_1, p_2, p_3, p_4, p_5, Q_1, Q_2, Q_3, Q_4) = \left[B_V^{-\sigma_1-\sigma_3+}(p_1, p_2, p_3, p_4, p_5, Q_1, Q_2, Q_3, Q_4) \right]^* \Big|_{P_V^* \rightarrow P_V}. \quad (\text{A.9})$$

A.2 The non-factorizable corrections

A general discussion for the photonic non-factorizable corrections for a process involving massless external particles and an arbitrary number of resonances can be found in [31]. Applying the general results displayed there to our processes, the correction factor results in

$$\begin{aligned} \delta_{\text{nfac}}^{\text{virt}}(\Phi_0^{\text{osh}}, (p_3 + p_4)^2 - M_V^2) = & \\ \sum_{i=1,2} \sum_{j=3,4} \tau_i \tau_j Q_i Q_j \frac{\alpha}{\pi} \text{Re} \left\{ \Delta^V(p_i^{\text{osh}}; (p_3 + p_4), p_j^{\text{osh}}) \right\}, & \\ V = W, Z & \end{aligned} \quad (\text{A.10})$$

with

$$\begin{aligned} \Delta^V(p_i^{\text{osh}}; (p_3 + p_4), p_j^{\text{osh}}) = & \\ 2 \ln \left(\frac{m_\gamma M_V}{M_V^2 - iM_V \Gamma_V - (p_3 + p_4)^2} \right) & \\ \times \left[\ln \left(\frac{\hat{t}}{t} \right) - 1 \right] - 2 - \text{Li}_2 \left(1 - \frac{\hat{t}}{t} \right). & \end{aligned} \quad (\text{A.11})$$

The kinematical variables \hat{t} and t are defined by

$$t = (p_i^{\text{osh}} - p_j^{\text{osh}})^2, \quad \hat{t} = (p_i^{\text{osh}} - p_3^{\text{osh}} - p_4^{\text{osh}})^2 - M_V^2, \quad (\text{A.12})$$

and Li_2 denotes the dilogarithm (21).

A.3 The real QED corrections

The determination of the helicity amplitudes for the real QED corrections can be performed in the same way as described in Appendix A.1 for the case of the Born amplitudes. The calculation is much more involved, though, since the set of generic diagrams comprises here 31 instead of five diagrams. These diagrams can be obtained from the ones shown in Fig. 5 in the following way. A total number of thirty diagrams is obtained by attaching the additional real photon to each fermion line and to each massive vector-boson line in the Born graphs shown in Fig. 5. The one remaining diagram results from both photons coupling to the intermediate vector boson via a $VV\gamma\gamma$ coupling. Apart from the increased number of diagrams, one has to calculate the generic amplitude for two different polarization combinations, since a final state with both photons having the same helicity is not related by any discrete symmetry to a final state with two photons of opposite helicity.

Adopting the conventions of Appendix A.1, the generic amplitude of the QED bremsstrahlung process reads

$$\begin{aligned} \mathcal{M}_{\text{real,QED}}^{\sigma_1\sigma_2\sigma_3\sigma_4\lambda_5\lambda_6}(p_1, p_2, p_3, p_4, p_5, p_6) = & \\ -4e^4 \delta_{c_1 c_2} \delta_{\sigma_1 - \sigma_2} \delta_{\sigma_3 - \sigma_4} \sum_V C_{V\bar{q}_2 q_1}^{\sigma_1} C_{V f_3 f_4}^{\sigma_3} & \\ \times B_{V\gamma}^{\sigma_1\sigma_3\lambda_5\lambda_6}(p_1, p_2, p_3, p_4, p_5, p_6, Q_{q_1}, Q_{q_2}, Q_{f_3}, Q_{f_4}), & \end{aligned} \quad (\text{A.13})$$

where the sum over V is again taken over all SM vector bosons. The couplings of the gauge boson V to the fermion f_a and the antifermion \bar{f}_b is again denoted by $C_{V\bar{f}_b f_a}^{\sigma}$ and can be read off Table 5. The generic function for all helicities positive is obtained as

$$\begin{aligned} B_{V\gamma}^{++++}(p_1, p_2, p_3, p_4, p_5, p_6, Q_1, Q_2, Q_3, Q_4) = & \\ \frac{\langle p_4 p_1 \rangle^2}{\langle p_4 p_5 \rangle \langle p_4 p_6 \rangle} \left\{ P_V(p_3 + p_4) \left[\frac{-Q_1^2 \langle p_3 p_2 \rangle^* \langle p_4 p_1 \rangle}{\langle p_1 p_5 \rangle \langle p_1 p_6 \rangle} \right. \right. & \\ + \frac{Q_1 Q_2 \langle p_4 | p_2 + p_5 | p_3 \rangle}{\langle p_2 p_5 \rangle \langle p_1 p_6 \rangle} + \frac{Q_1 Q_2 \langle p_4 | p_2 + p_6 | p_3 \rangle}{\langle p_1 p_5 \rangle \langle p_2 p_6 \rangle} & \\ + \frac{Q_2^2 \langle p_1 p_3 \rangle^* \langle p_2 p_4 \rangle}{\langle p_2 p_5 \rangle \langle p_2 p_6 \rangle} \Big] + P_V(p_3 + p_4 + p_5) & \\ \times \left[\frac{Q_3}{\langle p_3 p_5 \rangle} + P_V(p_3 + p_4) (Q_2 - Q_1) \langle p_5 p_3 \rangle^* \right] & \\ \times \left[\frac{Q_1 \langle p_4 | p_1 + p_6 | p_2 \rangle}{\langle p_1 p_6 \rangle} + \frac{Q_2 \langle p_4 | p_2 + p_6 | p_1 \rangle}{\langle p_2 p_6 \rangle} \right. & \\ \left. - P_V(p_1 + p_2) (Q_2 - Q_1) \langle p_1 p_2 \rangle^* \langle p_4 | p_2 + p_1 | p_6 \rangle \right] & \end{aligned}$$

$$\begin{aligned}
& + P_V(p_3 + p_4 + p_6) \\
& \times \left[\frac{Q_3}{\langle p_3 p_6 \rangle} + P_V(p_3 + p_4)(Q_2 - Q_1)\langle p_6 p_3 \rangle^* \right] \\
& \times \left[\frac{Q_1 \langle p_4 | p_1 + p_5 | p_2 \rangle}{\langle p_1 p_5 \rangle} + \frac{Q_2 \langle p_4 | p_2 + p_5 | p_1 \rangle}{\langle p_2 p_5 \rangle} \right. \\
& \left. - P_V(p_1 + p_2)(Q_2 - Q_1)\langle p_1 p_2 \rangle^* \langle p_4 | p_2 + p_1 | p_5 \rangle \right] \\
& - P_V(p_1 + p_2) \frac{Q_3^2}{\langle p_3 p_5 \rangle \langle p_3 p_6 \rangle} \langle p_1 p_2 \rangle^* \langle p_3 p_4 \rangle \Big\}, \tag{A.14}
\end{aligned}$$

where in the above expressions, a product like $\langle p_1 | p_4 + p_6 | p_5 \rangle$ is defined by

$$\langle a | b + c | d \rangle = \langle ab \rangle \langle db \rangle^* + \langle ac \rangle \langle dc \rangle^*. \tag{A.15}$$

The corresponding function for helicity λ_5 negative reads

$$\begin{aligned}
B_{V\gamma}^{+-+}(p_1, p_2, p_3, p_4, p_5, p_6, Q_1, Q_2, Q_3, Q_4) = & \\
& \frac{1}{\langle p_4 p_6 \rangle \langle p_3 p_5 \rangle^*} \\
& \times \left\{ P_V(p_3 + p_4) \left[\frac{Q_1^2}{\langle p_1 p_5 \rangle^* \langle p_1 p_6 \rangle} \frac{\langle p_3 p_2 \rangle^*}{(p_1 + p_5 + p_6)^2} \right. \right. \\
& \times \left(\langle p_4 | p_1 + p_5 | p_3 \rangle \langle p_4 | p_1 + p_5 | p_6 \rangle \langle p_1 p_6 \rangle \right. \\
& \left. \left. + \langle p_1 p_4 \rangle \langle p_1 p_5 \rangle^* \langle p_1 p_5 \rangle \langle p_2 p_4 \rangle \langle p_3 p_2 \rangle^* \right) \right. \\
& + \frac{Q_2^2}{\langle p_2 p_5 \rangle^* \langle p_2 p_6 \rangle} \frac{\langle p_4 p_1 \rangle}{(p_2 + p_5 + p_6)^2} \\
& \times \left(\langle p_5 | p_2 + p_6 | p_3 \rangle \langle p_4 | p_2 + p_6 | p_3 \rangle \langle p_2 p_5 \rangle^* \right. \\
& \left. \left. + \langle p_1 p_3 \rangle^* \langle p_2 p_6 \rangle^* \langle p_2 p_6 \rangle \langle p_2 p_3 \rangle^* \langle p_4 p_1 \rangle \right) \right. \\
& + \frac{Q_1 Q_2}{\langle p_2 p_5 \rangle^* \langle p_1 p_6 \rangle} \langle p_4 p_1 \rangle^2 (\langle p_2 p_3 \rangle^*)^2 \\
& \left. - \frac{Q_1 Q_2}{\langle p_1 p_5 \rangle^* \langle p_2 p_6 \rangle} \langle p_4 | p_1 + p_5 | p_3 \rangle^2 \right] \\
& + P_V(p_3 + p_4 + p_5) \langle p_1 | p_4 + p_5 | p_3 \rangle \\
& \times \left[\frac{Q_4}{\langle p_4 p_5 \rangle^*} - P_V(p_3 + p_4)(Q_2 - Q_1)\langle p_5 p_4 \rangle \right] \\
& \times \left[\frac{Q_1}{\langle p_1 p_6 \rangle} \langle p_4 p_1 \rangle \langle p_3 p_2 \rangle^* - \frac{Q_2}{\langle p_2 p_6 \rangle} \langle p_4 | p_2 + p_6 | p_3 \rangle \right. \\
& \left. + P_V(p_1 + p_2)(Q_2 - Q_1) \left(\langle p_6 p_2 \rangle^* \langle p_6 p_3 \rangle^* \langle p_6 p_4 \rangle \right. \right. \\
& \left. \left. + \langle p_4 | p_2 + p_1 | p_6 \rangle \langle p_3 p_2 \rangle^* \right) \right] \\
& + P_V(p_3 + p_4 + p_6) \langle p_4 | p_3 + p_6 | p_2 \rangle
\end{aligned}$$

$$\begin{aligned}
& \times \left[\frac{Q_3}{\langle p_3 p_6 \rangle} + P_V(p_3 + p_4)(Q_2 - Q_1)\langle p_6 p_3 \rangle^* \right] \\
& \times \left[\frac{Q_1}{\langle p_1 p_5 \rangle^*} \langle p_4 | p_2 + p_6 | p_3 \rangle + \frac{Q_2}{\langle p_2 p_5 \rangle^*} \langle p_4 p_1 \rangle \langle p_3 p_2 \rangle^* \right. \\
& \left. - P_V(p_1 + p_2)(Q_2 - Q_1) \left(\langle p_5 p_1 \rangle \langle p_5 p_4 \rangle \langle p_5 p_3 \rangle^* \right. \right. \\
& \left. \left. + \langle p_5 | p_2 + p_1 | p_3 \rangle \langle p_4 p_1 \rangle \right) \right] \\
& + P_V(p_1 + p_2) \left[P_V(p_3 + p_4)(Q_2 - Q_1)^2 \right. \\
& \times \langle p_1 p_4 \rangle \langle p_2 p_3 \rangle^* \langle p_4 p_5 \rangle \langle p_6 p_3 \rangle^* \\
& + \frac{Q_3^2}{\langle p_3 p_6 \rangle} \frac{\langle p_6 p_4 \rangle \langle p_3 p_6 \rangle^* \langle p_4 p_1 \rangle}{(p_3 + p_5 + p_6)^2} \langle p_5 | p_3 + p_6 | p_2 \rangle \\
& + \frac{Q_3 Q_4}{\langle p_3 p_6 \rangle \langle p_4 p_5 \rangle^*} \langle p_1 | p_4 + p_5 | p_3 \rangle \langle p_4 | p_3 + p_6 | p_2 \rangle \\
& \left. \left. - \frac{Q_4^2}{\langle p_4 p_5 \rangle^*} \frac{\langle p_5 p_3 \rangle^* \langle p_3 p_2 \rangle^* \langle p_5 p_4 \rangle}{(p_4 + p_5 + p_6)^2} \langle p_1 | p_4 + p_5 | p_6 \rangle \right] \right\}. \tag{A.16}
\end{aligned}$$

The other helicity combinations can be calculated by

$$\begin{aligned}
B_{V\gamma}^{-+\lambda_5+}(p_1, p_2, p_3, p_4, p_5, p_6, Q_1, Q_2, Q_3, Q_4) = & \\
& B_{V\gamma}^{++\lambda_5+}(p_2, p_1, p_3, p_4, p_5, p_6, -Q_2, -Q_1, Q_3, Q_4), \\
B_{V\gamma}^{+-\lambda_5+}(p_1, p_2, p_3, p_4, p_5, p_6, Q_1, Q_2, Q_3, Q_4) = & \\
& B_{V\gamma}^{++\lambda_5+}(p_1, p_2, p_4, p_3, p_5, p_6, Q_1, Q_2, -Q_4, -Q_3), \\
B_{V\gamma}^{-\lambda_5+}(p_1, p_2, p_3, p_4, p_5, p_6, Q_1, Q_2, Q_3, Q_4) = & \\
& B_{V\gamma}^{++\lambda_5+}(p_2, p_1, p_4, p_3, p_5, p_6, -Q_2, -Q_1, -Q_4, -Q_3), \tag{A.17}
\end{aligned}$$

and

$$\begin{aligned}
B_{V\gamma}^{\sigma_1 \sigma_3 \lambda_5 -}(p_1, p_2, p_3, p_4, p_5, p_6, Q_1, Q_2, Q_3, Q_4) = & \\
& \left[B_{V\gamma}^{-\sigma_1 - \sigma_3 - \lambda_5 +} \right. \\
& \left. (p_1, p_2, p_3, p_4, p_5, p_6, Q_1, Q_2, Q_3, Q_4) \right]^* \Big|_{P_V^* \rightarrow P_V}. \tag{A.18}
\end{aligned}$$

Appendix B: Explicit form of the (Lorentz-invariant) on-shell projection

In order to be able to evaluate the virtual corrections to the processes (3) in LPA, an on-shell projection has to be specified which maps a general set of momenta Φ_0 on a set of momenta Φ_0^{sh} such that $(p_3^{\text{sh}} + p_4^{\text{sh}})^2 = M_V^2$, where M_V is the mass of the decaying vector boson $V = W, Z$. Such

a projection is given by

$$\tilde{p}_3 = y_1 p_3, \quad \tilde{p}_5 = y_2 p_5, \quad \tilde{p}_4 = p_1 + p_2 - \tilde{p}_3 - \tilde{p}_5, \quad (\text{B.1})$$

where scaling variables y_1 and y_2 are obtained from the mass-shell conditions for the resonance and for the momentum \tilde{p}_4 as

$$y_2 = \frac{\hat{s} - M_V^2}{2(p_1 + p_2)p_5}, \quad y_1 = \frac{M_V^2}{2(p_1 + p_2 - zp_5)p_3}. \quad (\text{B.2})$$

This on-shell projection only involves Lorentz-invariant quantities.

References

1. The LEP collaborations ALEPH, DELPHI, L3, OPAL, LEP EWWG, SLD Heavy Flavor, Electroweak Groups, hep-ex/0412015 (2004)
2. S. Villa, Nucl. Phys. Proc. Suppl. **142**, 391 (2005) [hep-ph/0410208]
3. U. Baur, S. Errede, G. Landsberg, Phys. Rev. D **50**, 1917 (1994) [hep-ph/9402282]
4. A. Askew, Measurement of the $W\gamma \rightarrow \mu\nu\gamma$ cross section, limits on anomalous trilinear vector boson couplings, and the radiation amplitude zero in p anti- p collisions at $\sqrt{s} = 1.96$ TeV, PhD thesis, Rice University (2004), FERMILAB-THESIS-2004-31
5. M. Kirby, Measurement of $W + \gamma$ production in proton-antiproton collisions at $\sqrt{s} = 1.96$ TeV, PhD thesis, Duke University (2004), FERMILAB-THESIS-2004-32
6. N. Arkani-Hamed, S. Dimopoulos, G. Dvali, Phys. Lett. B **429**, 263 (1998) [hep-ph/9803315]
7. E. Mirabelli, M. Perelstein, M. Peskin, Phys. Rev. Lett. **82**, 2236 (1999) [hep-ph/9811337]
8. G. Giudice, R. Rattazzi, J. Wells, Nucl. Phys. B **544**, 3 (1999) [hep-ph/9811291]
9. DELPHI Collaboration, J. Abdallah et al., Eur. Phys. J. C **38**, 395 (2005) [hep-ex/0406019]
10. CDF Collaboration, D. Acosta et al., Phys. Rev. Lett. **89**, 281801 (2002) [hep-ex/0205057]
11. CDF II Collaboration, D. Acosta et al., Phys. Rev. Lett. **94**, 041803 (2005) [hep-ex/0410008]
12. D0 Collaboration, V.M. Abazov et al., Phys. Rev. Lett. **95**, 051802 (2005) [hep-ex/0502036]
13. D0 Collaboration, V. Abazov et al., Phys. Rev. Lett. **95**, 141802 (2005) [hep-ph/0504019]
14. S. Haywood et al., hep-ph/0003275 (1999)
15. J. Smith, D. Thomas, W.L. van Neerven, Z. Phys. C **44**, 267 (1989)
16. J. Ohnemus, Phys. Rev. D **47**, 940 (1993)
17. U. Baur, T. Han, J. Ohnemus, Phys. Rev. D **48**, 5140 (1993) [hep-ph/9305314]
18. J. Ohnemus, Phys. Rev. D **51**, 1068 (1995) [hep-ph/9407370]
19. U. Baur, T. Han, J. Ohnemus, Phys. Rev. D **57**, 2823 (1998) [hep-ph/9710416]
20. L.J. Dixon, Z. Kunszt, A. Signer, Nucl. Phys. B **531**, 3 (1998) [hep-ph/9803250]
21. D. De Florian, A. Signer, Eur. Phys. J. C **16**, 105 (2000) [hep-ph/0002138]
22. L. Dixon, Z. Kunszt, A. Signer, Phys. Rev. D **60**, 114037 (1999) [hep-ph/9907305]
23. J. Campbell, R. Ellis, Phys. Rev. D **60**, 113006 (1999) [hep-ph/9905386]
24. W. Beenakker et al., Nucl. Phys. B **410**, 245 (1993)
25. M. Beccaria et al., Phys. Rev. D **58**, 093014 (1998) [hep-ph/9805250]
26. P. Ciafaloni, D. Comelli, Phys. Lett. B **446**, 278 (1999) [hep-ph/9809321]
27. J.H. Kühn, A.A. Penin, hep-ph/9906545 (1999)
28. M. Melles, Phys. Rept. **375**, 219 (2003) [hep-ph/0104232]
29. E. Accomando, A. Denner, S. Pozzorini, Phys. Rev. D **65**, 073003 (2002) [hep-ph/0110114]
30. W. Hollik, C. Meier, Phys. Lett. B **590**, 69 (2004) [hep-ph/0402281]
31. E. Accomando, A. Denner, A. Kaiser, Nucl. Phys. B **706**, 325 (2005) [hep-ph/0409247]
32. A. Denner et al., Nucl. Phys. B **587**, 67 (2000) [hep-ph/0006307]
33. U. Baur, S. Keller, D. Wackerth, Phys. Rev. D **59**, 013002 (1999) [hep-ph/9807417]
34. S. Dittmaier, M. Krämer, Phys. Rev. D **65**, 073007 (2002) [hep-ph/0109062]
35. A. Martin et al., Eur. Phys. J. C **39**, 155 (2005) [hep-ph/0411040]
36. H. Spiesberger, Phys. Rev. D **52**, 4936 (1995) [hep-ph/9412286]
37. M. Roth, S. Weinzierl, Phys. Lett. B **590**, 190 (2004) [hep-ph/0403200]
38. S. Dittmaier, Nucl. Phys. B **565**, 69 (2000) [hep-ph/9904440]
39. S. Catani, M. Seymour, Phys. Lett. B **378**, 287 (1996) [hep-ph/9602277]
40. S. Catani, M. Seymour, Nucl. Phys. B **485**, 291 (1997) [hep-ph/9605323]
41. S. Catani, M. Seymour, Nucl. Phys. B **510**, 503 (1997) [hep-ph/9605323], Erratum
42. R. Stuart, Phys. Lett. B **262**, 113 (1991)
43. A. Aeppli, G. van Oldenborgh, D. Wyler, Nucl. Phys. B **428**, 126 (1994) [hep-ph/9312212]
44. A. Aeppli, F. Cuypers, G. van Oldenborgh, Phys. Lett. B **314**, 413 (1993) [hep-ph/9303236]
45. U. Baur, D. Zeppenfeld, Phys. Rev. Lett. **75**, 1002 (1995) [hep-ph/9503344]
46. W. Beenakker et al., Nucl. Phys. B **500**, 255 (1997) [hep-ph/9612260]
47. W. Beenakker, F. Berends, A. Chapovsky, Nucl. Phys. B **548**, 3 (1999) [hep-ph/9811481]
48. A. Denner et al., Nucl. Phys. B **560**, 33 (1999) [hep-ph/9904472]
49. G. Passarino, Nucl. Phys. B **574**, 451 (2000) [hep-ph/9911482]
50. E. Accomando, A. Ballestrero, E. Maina, Phys. Lett. B **479**, 209 (2000) [hep-ph/9911489]
51. W. Beenakker, F. Berends, A.P. Chapovsky, Nucl. Phys. B **573**, 503 (2000) [hep-ph/9909472]
52. W. Beenakker et al., Nucl. Phys. B **667**, 359 (2003) [hep-ph/0303105]
53. M. Beneke et al., Nucl. Phys. B **686**, 205 (2004) [hep-ph/0401002]

54. M. Beneke et al., Phys. Rev. Lett. **93**, 011602 (2004) [hep-ph/0312331]
55. M. Roth, Precise predictions for four-fermion production in electron positron annihilation, PhD thesis, ETH Zürich No. 13363 (1999) [hep-ph/0008033]
56. E. Argyres et al., Phys. Lett. B **358**, 339 (1995) [hep-ph/9507216]
57. A. Denner et al., Phys. Lett. B **612**, 223 (2005) [hep-ph/0502063]
58. A. Denner et al., Nucl. Phys. B **724**, 247 (2005) [hep-ph/0505042]
59. T. Hahn, Comput. Phys. Commun. **140**, 418 (2001) [hep-ph/0012260]
60. T. Hahn, Nucl. Phys. Proc. Suppl. **89**, 231 (2000) [hep-ph/0005029]
61. S. Dittmaier, M. Roth, Nucl. Phys. B **642**, 307 (2002) [hep-ph/0206070]
62. T. Hahn, Nucl. Phys. Proc. Suppl. **135**, 333 (2004) [hep-ph/0406288]
63. F.A. Berends, P.H. Daverveldt, R. Kleiss, Nucl. Phys. B **253**, 441 (1985)
64. F.A. Berends, P.H. Daverveldt, R. Kleiss, Comput. Phys. Commun. **40**, 285 (1986)
65. J. Hilgart, R. Kleiss, F. Le Diberder, Comput. Phys. Commun. **75**, 191 (1993)
66. F.A. Berends, R. Pittau, R. Kleiss, Nucl. Phys. B **424**, 308 (1994) [hep-ph/9404313]
67. R. Kleiss, R. Pittau, Comput. Phys. Commun. **83**, 141 (1994) [hep-ph/9405257]
68. S. Eidelman et al., Phys. Lett. B **592**, 1 (2004)
69. CDF Collaborattion, P. Azzi et al., hep-ex/0404010 (2004)
70. A. Denner, Fortschr. Phys. **41**, 307 (1993)
71. J. Pumplin et al., JHEP **07**, 012 (2002) [hep-ph/0201195]
72. U. Baur, D. Wackeroth, Phys. Rev. D **70**, 073015 (2004) [hep-ph/0405191]
73. ATLAS Collaboration, A. Airapetian et al., CERN-LHCC-99-14
74. T. Stelzer, W. Long, Comput. Phys. Commun. **81**, 357 (1994) [hep-ph/9401258]
75. H. Murayama, I. Watanabe, K. Hagiwara, KEK-91-11
76. A. Ballestrero, hep-ph/9911318
77. A. Ballestrero, E. Maina, Phys. Lett. B **350**, 225 (1995) [hep-ph/9403244]
78. S. Pozzorini, Electroweak radiative corrections at high energies, PhD thesis, Zürich University (2001) [hep-ph/0201077]
79. A. Denner, S. Pozzorini, Eur. Phys. J. C **18**, 461 (2001) [hep-ph/0010201]
80. A. Denner, S. Pozzorini, Eur. Phys. J. C **21**, 63 (2001) [hep-ph/0104127]
81. G. van Oldenborgh, J. Vermaseren, Z. Phys. C **46**, 425 (1990)
82. G. van Oldenborgh, Comput. Phys. Commun. **66**, 1 (1991)
83. H. Weyl, The Theory of Groups and Quantum Mechanics (Dover, New York, 1931)
84. B. van der Waerden, Group Theory and Quantum Mechanics (Springer, Berlin, 1974)
85. S. Dittmaier, Phys. Rev. D **59**, 016007 (1999) [hep-ph/9805445]